Chapter 5
ALE Formulation for Fluid-structure Interactions

The following paragraphs will be devoted to the Arbitrary Lagrangian Eulerian (ALE) method for modeling fluid-structure interactions. Based on the equations derived in Sect. 3.5, we describe methods for discretization in time and space. The basic techniques have already been introduced in Chap. 4, such that we can focus on the special characteristics of the Arbitrary Lagrangian Eulerian formulation for fluid-structure interaction problems.

In this chapter, we will focus on a strict interpretation of the ALE formulation for the Navier-Stokes system

$$\left.\begin{aligned} J\rho_f\Big(\partial_t \mathbf{v} + \mathbf{F}^{-1}(\mathbf{v} - \partial_t \mathbf{u}) \cdot \nabla \mathbf{v}\Big) - \operatorname{div}\Big(J\boldsymbol{\sigma}_f \mathbf{F}^{-T}\Big) &= J\rho_f \mathbf{f}, \\ \operatorname{div}\Big(J\mathbf{F}^{-1}\mathbf{v}\Big) &= 0, \end{aligned}\right\} \quad \text{in } \hat{\mathcal{F}},$$

where the set of equations is completely mapped onto the reference coordinate system in $\hat{\mathcal{F}}$, see [126, 199, 201, 285]. In literature an alternative formulation is often discussed [48, 120, 140, 147, 181, 221]. The problem is there mapped back into the Eulerian coordinate system and reads

$$\left.\begin{aligned} \rho_f\Big(\partial_t \mathbf{v} + (\mathbf{v} - \partial_t \mathbf{u}) \cdot \nabla \mathbf{v}\Big) - \operatorname{div}\ \boldsymbol{\sigma}_f &= \rho_f \mathbf{f}, \\ \operatorname{div}\ \mathbf{v} &= 0. \end{aligned}\right\} \quad \text{in } \mathcal{F}(t).$$

The domain mapping only enters via the additional transport term. The benefit of this presentation is the simplicity of formulation. After every time step, the mesh must be updated. Considering time stepping schemes, where the solution and the domain motion enters at two distinct points in time at once, the derivation of accurate higher order schemes is less obvious using this second formulation. From a theoretical point of view, both formulations are equivalent. Whether one uses a fixed mesh and the reference formulation or a moving mesh and the Eulerian formulation,

T. Richter, *Fluid-structure Interactions*, Lecture Notes in Computational Science and Engineering 118, DOI 10.1007/978-3-319-63970-3_5

both problems give the same result. Considering strictly monolithically coupled schemes, the first ALE formulation is more natural, as it allows for a variational coupling of the two different sub-systems, see Sect. 3.5.

5.1 Time-Discretization for the FSI Problem in ALE-Formulation

Time discretization of fluid-structure interactions is mainly governed by two specific complexities. First, the overall stiffness of the coupled problem is by far greater than that of the two single subproblems. This is mainly due to the coupling of a parabolic type fluid equations with the solid equations of hyperbolic type. Second the ALE time derivative of the domain acts as transport direction for the fluid field. This gives rise to nonlinear couplings of temporal and spatial derivatives, which is very uncommon for most partial differential equations.

We start by repeating the coupled system of equations describing fluid-structure interactions in Arbitrary Lagrangian coordinates. Compare to Problem 3.11:

$$\begin{aligned}
\left(J(\partial_t \mathbf{v} + (\mathbf{F}^{-1}(\mathbf{v} - \partial_t \mathbf{u}) \cdot \nabla)\mathbf{v}, \phi\right)_{\mathcal{F}} + \left(J\boldsymbol{\sigma}_f \mathbf{F}^{-T}, \nabla\phi\right)_{\mathcal{F}} &= (J\rho_f \mathbf{f}, \phi)_{\mathcal{F}} \\
\left(J\mathbf{F}^{-1} : \nabla \mathbf{v}^T, \xi\right)_{\mathcal{F}} &= 0 \\
(\rho_s^0 \partial_t \mathbf{v}, \phi)_{\mathcal{S}} + (\mathbf{F}\boldsymbol{\Sigma}_s, \nabla\phi)_{\mathcal{S}} &= (\rho_s^0 \mathbf{f}, \phi)_{\mathcal{S}} \\
(\partial_t \mathbf{u} - \mathbf{v}, \psi_s)_{\mathcal{S}} &= 0 \\
(\nabla \mathbf{u}, \nabla \psi_s)_{\mathcal{F}} &= 0,
\end{aligned} \tag{5.1}$$

where we have reformulated the divergence condition in the fluid equations by means of Lemma 2.61 to ease implementation and to avoid the presence of second derivatives. For construction of the ALE map, we consider a simple harmonic extension, see Sect. 5.3.5 for variants. For simplicity of notation, we have skipped all hats that usually indicate use of Lagrangian or ALE coordinates. Apart from the strong nonlinearities, this equation has some special feature with respect to the temporal derivatives. These are not isolated but appear in coupling to spatial derivatives

$$\left(J\left(\partial_t \mathbf{v} - (\mathbf{F}^{-1}\partial_t \mathbf{u} \cdot \nabla)\mathbf{v}\right), \phi\right)_{\mathcal{F}} + \dots \tag{5.2}$$

A detailed analysis of fluid flows on moving domains has been performed by Formaggia and Nobile [143, 144]. These studies already tackle several important aspects such as stability and order of convergence. In fluid-structure interaction, the fluid-domain movement is caused by the solid deformation. Hence, the analysis of fully coupled fluid-structure interaction is similar but must also include a discussion on the solid discretization.

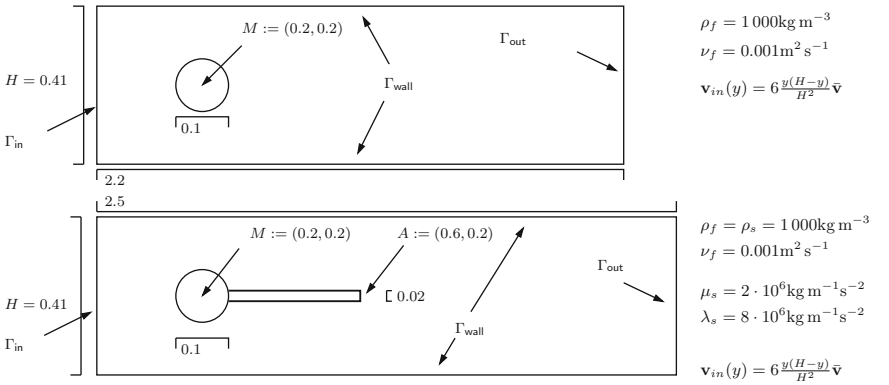

Fig. 5.1 Configuration of the two benchmark problems. The *upper figure* shows the cfd benchmark by Schäfer and Turek, the *lower figure* shows the layout of the fsi benchmark by Hron and Turek

5.1.1 Non-stationary Dynamics of Fluid-structure Interactions

We start the discussion on time-discretizations of fluid-structure interaction with a survey on results for two benchmark problems in fluid-dynamics and for fluid-structure interactions: In 1995, Schäfer and Turek [299] presented a benchmark configuration for incompressible laminar flows. In 2006, Hron and Turek [200] published results for a two dimensional fluid-structure interaction benchmark that has been constructed on top of the cfd benchmark problem. Both problems use the geometric configuration shown in Fig. 5.1. The main difference is an elastic beam that is attached to the rigid obstacle. Further, the domain of the fsi problem has been lengthened to avoid spurious feedback of the outflow boundary to the dynamics of the oscillation.

Both problems are driven by a prescribed inflow profile $\mathbf{v}^D$ on Γ_{in}. The full set of parameters for both problems is given by

$$\rho_f^{\text{cfd}} = 1\,\text{kg} \cdot \text{m}^{-3}, \quad \rho_f^{\text{fsi}} = 10^3\,\text{kg} \cdot \text{m}^{-3}$$

$$\nu_f^{\text{cfd/fsi}} = 10^{-3}\,\text{m}^2 \cdot \text{s}^{-1}, \quad \mathbf{v}^D(0, y) = 1.5\omega(t)\frac{y(H-y)}{(H/2)^2}\bar{\mathbf{v}},$$

where $\omega(t) = (1 - \cos(\pi t/2))$ for $t < 2\,\text{s}$ and $\omega(t) = 1$ for $t \geq 2\,\text{s}$ is used for regularizing the initial data. As average speed, we consider $\bar{\mathbf{v}} = 2\,\text{m} \cdot \text{s}^{-1}$. In the original cfd benchmark problem, $\bar{\mathbf{v}}^{\text{cfd}} = 1\,\text{m} \cdot \text{s}^{-1}$ was considered. With the radius of the obstacle $D = 0.1$, the Reynolds number is given by

$$Re = \frac{\bar{\mathbf{v}}D}{\nu} = 200.$$

The description of the problem is closed by providing the material parameters of the elastic solid

$$\rho_s^{\text{fsi}} = 10^3\,\text{kg}\cdot\text{m}^{-3}, \quad \mu_s = 2\cdot 10^6\,\text{kg}\cdot\text{m}^{-1}\text{s}^{-2}, \quad \lambda_s = 8\cdot 10^6\,\text{kg}\cdot\text{m}^{-1}\text{s}^{-2}.$$

As quantity of interest, we consider principal boundary stresses in x- and y-direction on the obstacle with boundary Γ_{obs}

$$\begin{aligned} J_{\text{drag}}(\mathbf{v},p) &= \frac{2}{\bar{\mathbf{v}}^2\rho_f L}\int_{\Gamma_{\text{obs}}} \boldsymbol{\sigma}_f \mathbf{n}\mathbf{e}_x \,\mathrm{d}o, \\ J_{\text{lift}}(\mathbf{v},p) &= \frac{2}{\bar{\mathbf{v}}^2\rho_f L}\int_{\Gamma_{\text{obs}}} \boldsymbol{\sigma}_f \mathbf{n}\mathbf{e}_y \,\mathrm{d}o. \end{aligned} \tag{5.3}$$

By Γ_{obs} we denote the boundary of the circle with diameter in the case of the cfd-benchmark and the circle with attached beam in the case of the fsi-benchmark problem. Efficient ways for evaluating these functionals are shown in [62, 282] as well as in Sect. 8.3.2.

Figure 5.2 shows the drag-coefficient (5.3) as function over time $I = [0, 5]$ for the two benchmark problems. Both configurations show a similar behavior with a transient initial phase leading to a periodic oscillation with dominant frequencies $f_{\text{cfd}} = 13\,\text{Hz}$ for the cfd benchmark and $f_{\text{fsi}} \approx 11\,\text{Hz}$ for the fsi problem. The first obvious difference is the longer transient phase for the fsi benchmark problem. An insight look into the subinterval $I' = [2.5, 3]$ reveals high frequent oscillations $f_{\text{high}} \approx 100\,\text{Hz}$ in the drag-coefficient with a small amplitude $a \approx 10^{-4}$ that is not visible on the large scale. These high frequent oscillations are no numerical artifacts but remain stable under temporal and spatial mesh refinement. They are only present in the coupled fsi system.

Reviewing the results published by many research groups in the two surveys on the cfd benchmark problem [299] and the fsi benchmark [199, 201] a first surprising

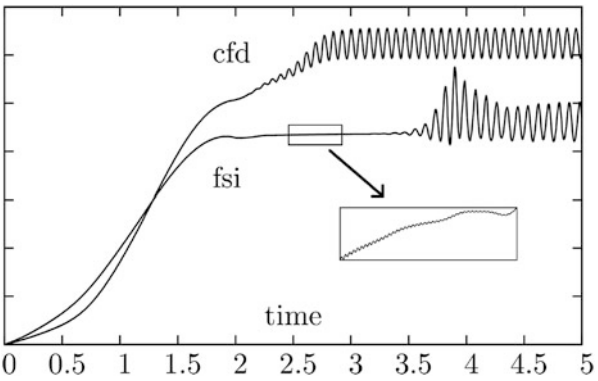

Fig. 5.2 Comparison of the two benchmark problems cfd and fsi. We plot the drag coefficient as function over time. For the fsi-problem we show a detailed view of the transient oscillations revealing high frequent modes

observation is the choice of discretization parameters that have been necessary to obtain approximations with appropriate accuracy: even though more than a decade lies between both benchmark problems, the dimension of the spatial discretization is very similar. In both cases, about 300,000 spatial degrees of freedom are sufficient to result in output values of about 1% accuracy. The increased difficulty of the fsi benchmark problem has been accounted for by a general use of higher order finite elements, where most contributors to the original cfd benchmark problem relied on lowest order finite elements. However, observing the temporal discretization, it is found that the fsi benchmark asks for significantly finer resolution in time. While less than 10 time steps per period of the oscillation were sufficient in the cfd case, accurate results to the fsi benchmark problem required up to 100 time steps per period of oscillation resulting in time steps as small as 10^{-3}. One explanation for this difference in temporal discretization can be found in the high frequent oscillations that are present with small amplitude, see Fig. 5.2.

Further insight is given by a discrete Fourier analysis of the output functional $J_{\text{drag}}(t)$ as function over time. We analyze few oscillation of the output functional with a very fine temporal resolution (down to $k \approx 10^{-5}$). Figure 5.3 reveals several dominant frequencies, at about 100 Hz (see also Fig. 5.2, 500 Hz and 800 Hz. These modes are stable under mesh refinement and further downscaling of the time step. The modes belonging to higher frequencies carry less energy. But even though the high frequent contributions take place on a much smaller scale as the dominant oscillation $f_{\text{fsi}} \approx 11\,\text{Hz}$, they must be carefully resolved to capture the overall dynamics of the coupled benchmark problem. The key question in this respect is the origin of these micro-oscillations. They are not present in pure fluid-dynamical simulations. A corresponding Fourier analysis of the fluid functions $J(\mathbf{v}, p)$ does not show any overtones. Further, they are no numerical artifact, but stable under discretization of both spatial and temporal discretization. Instead they stem from the coupling to the hyperbolic structure equations.

A further question to be investigated is the period of oscillations in coupled fluid-structure interaction systems. Figure 3.3 in Sect. 3.3 showed that the non-stationary dynamics of coupled fluid-structure systems can largely vary from pure fluid flows. Two geometrically similar problems at Reynolds number $Re = 140$ show a stationary behavior for a fixed and rigid body, whereas instationary oscillations appear for a flexible body. In laminar fluid-dynamics, the frequency of the Kármán vortex street depends on the Reynolds number of the flow, hence on the velocity. Structural systems have their own eigenmodes. Whether a coupled system is oscillating and which frequency and amplitude is obtained is not fully understood [250, 261]. We investigate this problem in Chap. 11.

5.1.2 Time Stepping Schemes for Fluid-structure Interactions

There is little theoretical background on monolithic time-discretizations of fluid-structure interactions. The main difficulty stems from the motion of the subdomains

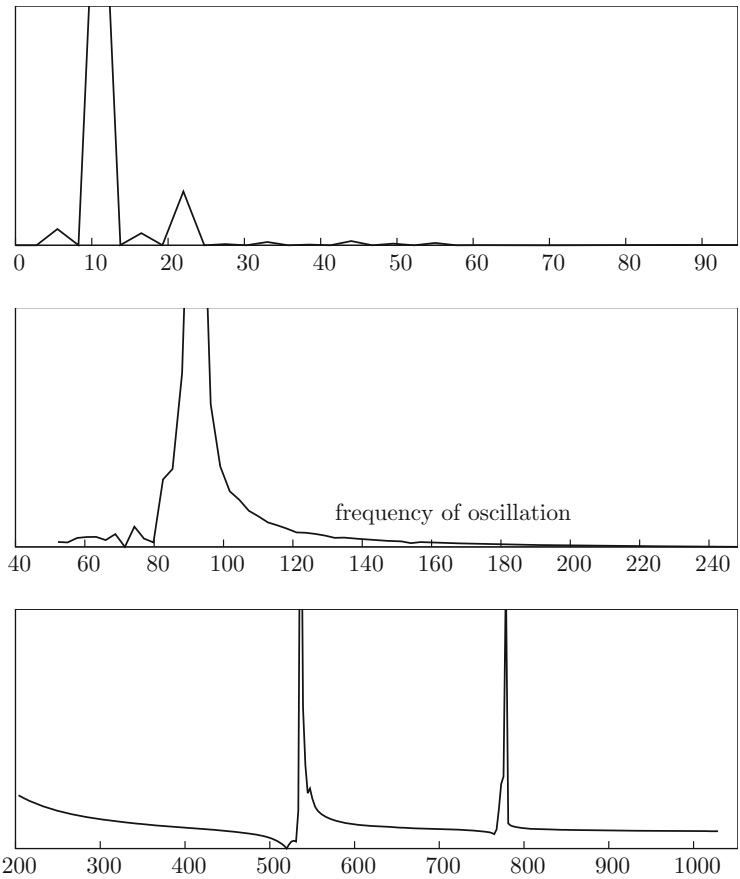

Fig. 5.3 Discrete Fourier analysis of the output functional (drag) shows the dominant frequency $f_{\text{fsi}} \approx 11\,\text{Hz}$ and further important sub-frequencies at about $f \approx 100\,\text{Hz}$ and $500\,\text{Hz}$ as well as $800\,\text{Hz}$. These modes are stable under temporal and spatial mesh refinement

that must either be modeled explicitly in partitioned approaches or that must be taken care of by implicit transformations of either the fluid-domain or the solid-domain. Concentrating first on pure fluid problems on moving domains, some crucial aspects with respect to stability and order of convergence are already identified by Formaggia and Nobile [143, 144]. In addition Fernández and Gerbeau [140] provide a stability analysis for fluid-structure interaction problems. Several studies with qualitative comparisons of different time stepping schemes and their long-time behavior have been reported in [342, 348]. In the primer study and additionally in [347] a detailed discussion on the practical realization and implementation of time stepping schemes for ALE fluid-structure interaction is given.

In the following, we put the attention on the strict variant of the ALE method that completely acts on the fixed reference domains $\mathcal{F}$ and $\mathcal{S}$, and where the complete set of equations is mapped.

Here, the domain motion is hidden in the ALE-map $T_f(x,t)$ and calls for the discretization of non-standard space-time coupled terms like, see (5.1) and (5.2):

$$(J(\mathbf{u})\nabla\mathbf{v}\mathbf{F}^{-1}(\mathbf{u})\partial_t\mathbf{u},\phi)_{\mathcal{F}}. \tag{5.4}$$

Most approaches for the temporal discretization of this term are ad hoc and based on the experience with other types of equations as Navier-Stokes of multiphase fluids, see [198].

5.1.2.1 Derivation of Second Order Time Stepping Schemes

The derivation of a second order stable time stepping scheme is not obvious. Specifically, regarding (5.4), two immediate reasonable choices for are given by the secant version

$$\left(\left[\frac{J(\mathbf{u}^{m-1})\nabla\mathbf{v}^{m-1}\mathbf{F}^{-1}(\mathbf{u}^{m-1})}{2}+\frac{J(\mathbf{u}^{m})\nabla\mathbf{v}^{m}\mathbf{F}^{-1}(\mathbf{u}^{m})}{2}\right]\frac{\mathbf{u}^m-\mathbf{u}^{m-1}}{k_m},\phi\right),$$

and the midpoint-tangent version

$$\left(\left[J(\bar{\mathbf{u}})\nabla\bar{\mathbf{v}}\mathbf{F}^{-1}(\bar{\mathbf{u}})\right]\frac{\mathbf{u}^m-\mathbf{u}^{m-1}}{k_m},\phi\right),$$

$$\bar{\mathbf{u}}:=\frac{\mathbf{u}^{m-1}+\mathbf{u}^m}{2},\quad \bar{\mathbf{v}}:=\frac{\mathbf{v}^{m-1}+\mathbf{v}^m}{2},$$

of the trapezoidal rule. This idea is explored in [343, 348].

A third version of a time stepping scheme can be derived by using a temporal $cG(1)/dG(0)$-Galerkin approach of (5.4) as described in Sect. 4.1.3. Using piecewise linear continuous trial spaces for all deformation $\mathbf{u}$ and velocity $\mathbf{v}$ in combination with piecewise constant globally discontinuous test spaces yields the time derivative term

$$\left(\left[\frac{1}{6}J(\mathbf{u}^{m-1})\nabla\mathbf{v}^{m-1}\mathbf{F}^{-1}(\mathbf{u}^{m-1})+\frac{2}{3}J(\bar{\mathbf{u}})\nabla\bar{\mathbf{v}}\mathbf{F}^{-1}(\bar{\mathbf{u}})\right.\right.$$
$$\left.\left.+\frac{1}{6}J(\mathbf{u}^{m})\nabla\mathbf{v}^{m}\mathbf{F}^{-1}(\mathbf{u}^{m})\right]\frac{\mathbf{u}^m-\mathbf{u}^{m-1}}{k_m},\phi\right),$$

where again by $\bar{\mathbf{u}}$ and $\bar{\mathbf{v}}$ we denote the average of old and new approximation. Such a Galerkin-derivation is also possible for more advanced time stepping schemes like the fractional step theta method, see [239, 240] and Sect. 4.1.2.

Simple truncation error analysis shows second order convergence for $k \to 0$ in all three cases. The leading error constants slightly differ:

$$C_1 \approx \frac{11}{8}, \quad C_2 \approx \frac{3}{8}, \quad C_3 \approx \frac{3}{4}.$$

In numerical experiments, it is found that all of these variants show very similar performance. Significant differences in temporal accuracy could not be found.

Finally, we point out that the Crank-Nicolson scheme applied to the elastic structure equation in mixed formulation is closely related to the Newmark scheme [23], which is one of the most prominent time-discretization techniques in solid mechanics.

5.1.2.2 Temporal Stability

Issues of numerical stability are of utter importance for fluid-structure interaction problems, as they consist of the coupled consideration of two different types of equations: the incompressible Navier-Stokes equations which is of parabolic type and that comes with smoothing properties and the hyper-elastic solid equation of hyperbolic type that calls for good conservation properties with very little numerical dissipation. By these considerations, the Crank-Nicolson scheme and its variants like shifted versions [230, 266] or the fractional step theta scheme [74, 328], appear to be ideal candidates. Further, both are second order accurate.

Motivated Heywood and Rannacher [187] and Formaggia and Nobile [144] it is reported in [140, 348] that the discretization of the domain-motion term (5.4) introduces further stability issues. To investigate this stability problem, we again consult the fsi benchmark problem introduced in the previous sections. Figure 5.4 shows the drag as functional over time for an unstable pair of spatial and temporal discretization parameters. Further, we also show the stable simulation using a damped version of the time stepping scheme.

In a first test, we aim at obtaining a stable solution up to $T = 10$. On a sequence of uniform meshes, we identify the largest time step k that is suited to generate a stable solution. The left part of Table 5.1 shows the results. Here, we see that on the coarsest mesh, the large step size $k = 0.02$ is sufficient, while on finer meshes $k < 0.004$ is required. We however cannot identify a direct relationship between mesh size and time step if we go to even finer spatial mesh resolutions.

In a second test case, we consider the (relatively large) step size $k = 0.005$ and $k = 0.00\bar{3}$ and determine the point in time $T_{\max}$, where the solution gets unstable. Again, we carry out this test case on different meshes. At first glance, the results in the right part of Table 5.1 for $k = 0.005$ suggest a stability relationship between time step and mesh size. The results concerning the second configuration with $k = 0.00\bar{3}$ however does not confirm this conjecture. Here, we can even reach a larger final point in time $T_{\max}$ on finer meshes. Further, the simulations on the finest mesh do

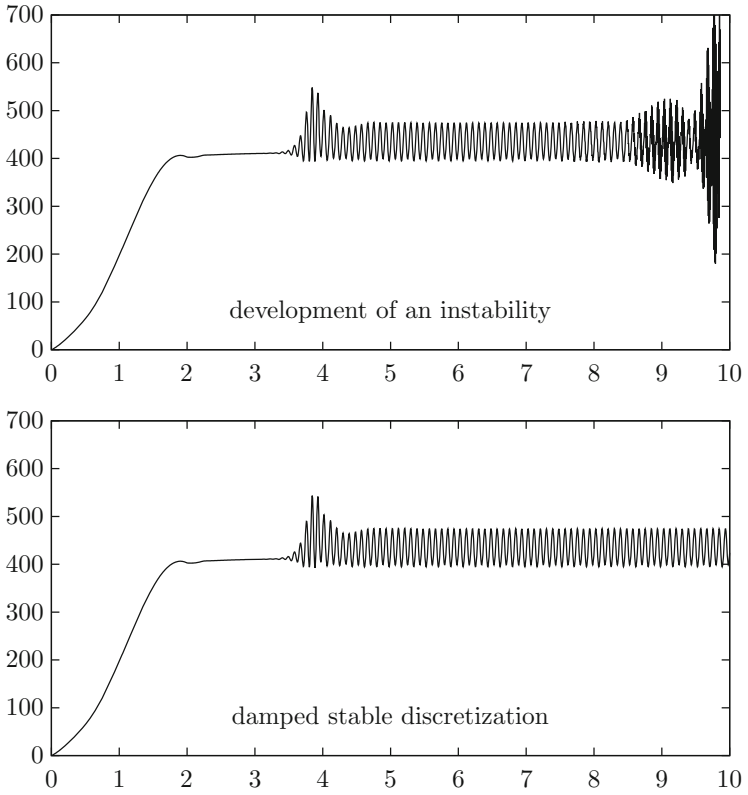

Fig. 5.4 Simulation for $k = 0.005$. *Top*: undamped Crank-Nicolson scheme develops an instability. *Bottom*: implicitly shifted scheme produces a stable solution on $I = [0, 10]$

Table 5.1 Long-term stability of the Crank-Nicolson scheme

	Time step size			
Mesh-Level	0.025	0.02	0.004	$0.00\bar{3}$
1	×	√	√	√
2	×	×	×	√
3	×	×	×	√

Mesh-Level	$k = 0.005$	$0.00\bar{3}$
1	$\gg 10$	$\gg 10$
2	8.48	10.82
3	6.04	12.54
4	3.84	3.84

Left: combination of time step k and mesh size h, such that the solution is stable in the interval $I = [0, 10]$. We cannot find a strict time step relation $k \leq h^{\alpha}$. Right: maximum interval $I = [0, T_{\max}]$, where a solution could be found for $k = 0.005$ and $k = 0.00\bar{3}$, depending on the mesh-size. Here, we also cannot identify an obvious relationship

not cease due to stability problems but due to early failure of the Newton scheme. Altogether, it is not possible to numerically certify a strict time step restriction. Instead we find a general stability problem for long-term simulations if we consider the Crank-Nicolson scheme.

5.1.2.3 Stable Time-Discretization and Damping

The analysis of the fsi benchmark problem shows that the restrictive time step condition is by stability and not by accuracy requirements. We will therefore discuss accurate time-discretization schemes with better stability properties. A possibility is to either resort to A-stable time-discretization schemes, or to apply modifications of the Crank-Nicolson schemes. Two possibilities are often discussed in literature: by a slight implicit shifting of the discretization we recover global stability, see [186, 187, 230] and also Sect. 4.1.2:

$$(u^m - u^{m-1}, \phi) + \left(\frac{1}{2} + O(k)\right) a(u^m, \phi) + \left(\frac{1}{2} - O(k)\right) a(u^{m-1}, \phi) = 0$$

This is sufficient for damping of accumulated errors by truncation, quadrature or inexact solution of the algebraic systems. If the shift depends on the time step size, the resulting scheme is still second order accurate in time. Similar results are recovered by applying some initial time steps with the A-stable backward Euler method, see [266]. If these few (usually two are sufficient) backward Euler steps are introduced after every fixed time-interval, e.g. at every $t = j$ for $j = 0, 1, \ldots$, we also recover sufficient stability for long term calculations. This scheme, also referred to as *Rannacher time-marching*, is second order accurate.

Higher stability that is also sufficient to cover non-smooth initial data is reached by applying strongly A-stable time-integration techniques. Here, the fractional-step theta method appears to be an optimal choice [74]. This time stepping scheme consists of three sub-steps that combined results in a second order, strongly A-stable scheme that further has very good dissipation properties. It is highly preferable to flow problems [328] and also frequently used in the analysis of fluid-structure interactions problems [198, 201, 287, 342].

In the following, we compare the three possibilities of a non-damped Crank-Nicolson scheme, with an implicitly shifted version using $\theta = \frac{1}{2} + k$ and the *Rannacher time-marching* algorithm with two steps of the backward Euler method at times $t = 0$, $t = 1$, $t = 2$ and so on. In Fig. 5.5 we compare these three damping strategies. We show the drag-coefficient (see Figs. 5.2 or 5.4 for a global view) in the sub-intervals $t \in [3.5, 4.2]$, $t \in [7.95, 8.15]$ and $t \in [9.3, 9.6]$. While all three versions are stable at initial time, *Rannacher time-marching* develops a first instability after two steps of backward Euler at time $t = 4$, see the upper sketch in Fig. 5.5. This instability will remain during the simulation, but it will not be further intensified, as can be seen in the middle and right sketch of the figure. The undamped version of the Crank-Nicolson scheme delivers stable solutions up to a moderate time of about $t = 5$ but develops a strong instability that will finally lead to a breakdown of the scheme, as can be seen in the middle and lower sketch. Finally, the implicitly shifted version of the Crank-Nicolson scheme gives stable and good results globally in time.

A systematic way for deriving a time stepping scheme is the detour using a Galerkin formulation. Here, we exemplarily derive the cG(1)-method that—for

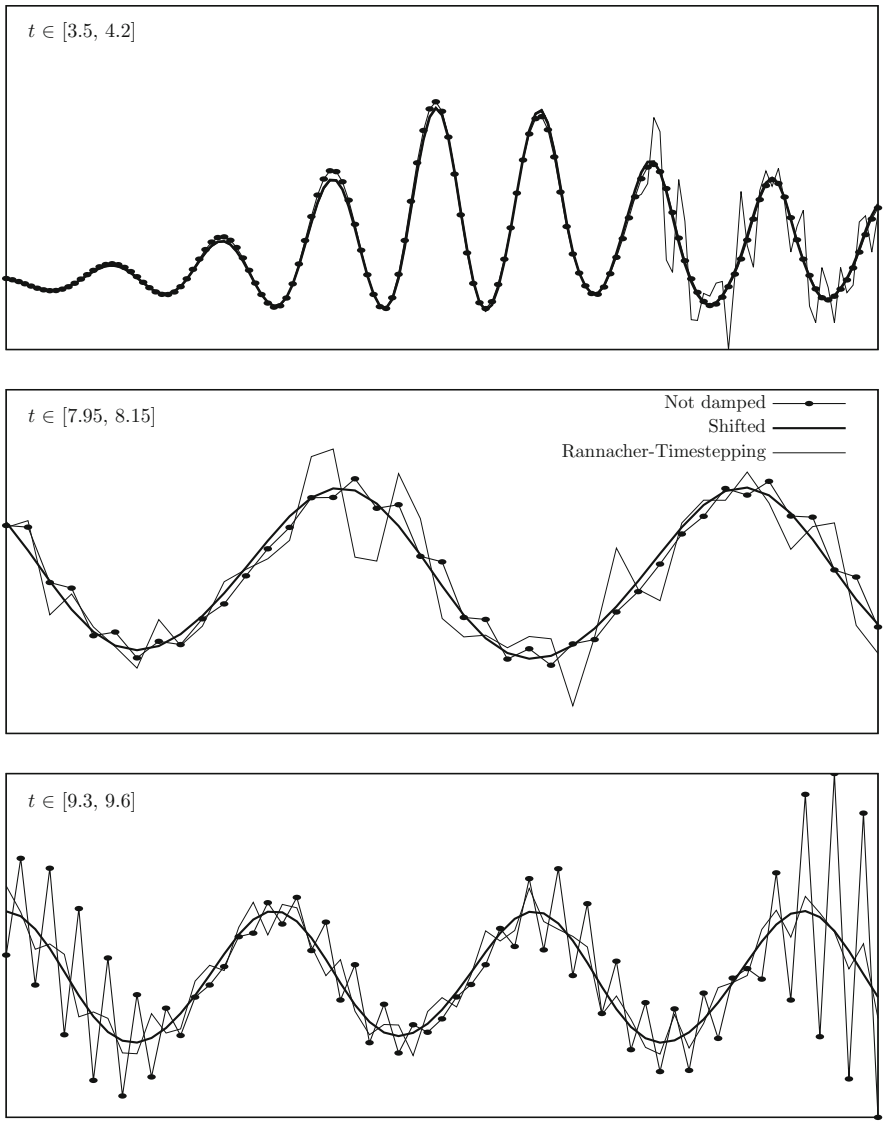

Fig. 5.5 Comparison of different damping strategies: undamped Crank-Nicolson, shifted version $\frac{1}{2} + k$ and Rannacher time-marching with two backward Euler steps at every time-unit

parabolic autonomous systems—is equivalent to the Crank-Nicolson scheme. We find $u_k, f_k, g_k \in X_I^1$ in the space of piece-wise linear, globally continuous functions and use $X_I^{0,\mathrm{dc}}$ as test space. On an interval I_m we write

$$f_k\big|_{I_m} = f_k^{m-1}\psi^{m-1} + f_k^m\psi^m, \quad g_k\big|_{I_m} = g_k^{m-1}\psi^{m-1} + g_k^m\psi^m,$$

where

$$\psi^{m-1}(t) = \frac{t_m - t}{t_m - t_{m-1}}, \quad \psi^m(t) = \frac{t - t_{m-1}}{t_m - t_{m-1}}.$$

5.2 Linearizations of Fluid-structure Interactions in the ALE Framework

Discretization in time results in a sequence of quasi-stationary systems of partial differential equations. These are highly nonlinear. Nonlinearities arise from material laws, convective terms and in the case of fluid-structure interactions due to the motion of the domain. Considering the strict ALE formulation with mapping of the complete variational system to a reference domain this domain nonlinearity is represented by the domain map T, its gradient $\mathbf{F}$ and determinant J. In the following paragraphs, we will discuss different ways to linearize these quasi-stationary systems. First of all, a straightforward way to linearize the set of equations would be the use of explicit time stepping schemes. This however is not feasible due to several reasons: first of all, the incompressibility constraint of the Navier-Stokes equations (or for incompressible solids) cannot be taken care of by explicit methods. Application of projection schemes would allow for explicit discretization of the momentum equations. We do not follow this approach, but refer to the literature [139, 262]. Another drawback of explicit discretization schemes is the limited stability that will call for very strict step-size conditions. The use of small time steps is a contrast to the benefits of monolithic schemes that allow for implicit discretizations with large time steps.

For the following we will consider implicit schemes only. Here we focus on time-discretization with the backward Euler method. Adaption to other single-step schemes is straightforward. Given velocity $\mathbf{v}^{\text{old}}$ and deformation $\mathbf{u}^{\text{old}}$ at previous time step we find (see Lemma 3.11)

$$\mathbf{v} \in \mathcal{V}, \quad \mathbf{u} \in \mathcal{W}, \quad p_f \in \mathcal{L}_f,$$

such that

$$\begin{aligned}
\left(\rho_f J \left(k^{-1}(\mathbf{v} - \mathbf{v}^{\text{old}}) + \mathbf{F}^{-1}(\mathbf{v} - k^{-1}(\mathbf{u} - \mathbf{u}^{\text{old}})) \cdot \nabla \mathbf{v}\right), \phi\right)_{\mathcal{F}} & \\
+ \left(J\boldsymbol{\sigma}_f \mathbf{F}^{-T}, \nabla\phi\right)_{\mathcal{F}} &= (J\rho_f \mathbf{f}, \phi)_{\mathcal{F}} \\
\left(J\mathbf{F}^{-1} : \nabla \mathbf{v}^T, \xi\right)_{\mathcal{F}} &= 0 \\
(\rho_s^0 k^{-1}(\mathbf{v} - \mathbf{v}^{\text{old}}), \phi)_{\mathcal{S}} + (\mathbf{F}\boldsymbol{\Sigma}_s, \nabla\phi)_{\mathcal{S}} &= (\rho_s^0 \mathbf{f}, \phi)_{\mathcal{S}} \\
(k^{-1}(\mathbf{u} - \mathbf{u}^{\text{old}}) - \mathbf{v}, \psi_s)_{\mathcal{S}} &= 0 \\
(\nabla \mathbf{u}, \nabla \psi_f)_{\mathcal{F}} &= 0,
\end{aligned} \tag{5.5}$$

for all

$$\phi \in \mathcal{V}, \quad \psi_f \in \mathcal{W}_f, \quad \psi_s \in \mathcal{L}_s, \quad \xi_f \in \mathcal{L}_f.$$

The fluid's stress tensor σ_f in ALE coordinates and the 2nd Piola Kirchhoff stress tensor of the St. Venant Kirchhoff material are given by

$$\begin{aligned} \boldsymbol{\sigma}_f &:= -pI + \rho_f \nu_f (\nabla \mathbf{v} \mathbf{F}^{-1} + \mathbf{F}^{-T} \nabla \mathbf{v}^T) \\ \boldsymbol{\Sigma}_s &:= 2\mu_s \mathbf{E}_s + \lambda_s \operatorname{tr}(\mathbf{E}_s) I, \end{aligned} \tag{5.6}$$

where the Green-Lagrangian Strain tensor is defined as

$$\mathbf{E}_s := \frac{1}{2}(\mathbf{F}^T \mathbf{F} - I).$$

Finally, we denote by $\rho_f, \rho_s^0, \nu_f, \mu_s$ and λ_s the material parameters describing density of fluid and solid, kinematic viscosity, shear modulus and Lamé coefficient.

We skipped all "hat's" denoting the use of reference coordinates. By $\mathcal{F}$ and $\mathcal{S}$ denote the fixed reference domains of fluid and solid. The function spaces $\mathcal{V}$ and $\mathcal{W}$ are basically the space $H^1(\Omega)^d$ differing only in the type of boundary values. While $\mathcal{W} = H_0^1(\Omega)^d$ has Dirichlet boundary values all around $\partial\Omega$, the velocity space $\mathcal{V} = H_0^1(\Omega; \Gamma^D)^d$ can have a Neumann outflow boundary $\Gamma_f^{\text{out}} \subset \partial\Omega$. The pressure space $\mathcal{L}_f = L^2(\mathcal{F})$ is defined on the fluid-domain only. The test space $\mathcal{W}_f = H_0^1(\mathcal{F})^d$ for the definition of the ALE-map has homogenous Dirichlet values all around the fluid-domain. The test space of the deformation-velocity relation is $\mathcal{L}_s = L^2(\mathcal{S})^d$.

5.2.1 Linearization by Fixed Point-Iterations

A simple approach to linearization of (5.5) is to apply fixed point-iterations. Starting with

$$\mathbf{v}^{(0)} = \mathbf{v}^{\text{old}}, \quad \mathbf{u}^{(0)} = \mathbf{u}^{\text{old}},$$

we search for approximations $\mathbf{v}^{(l)}$ and $\mathbf{u}^{(l)}$ that converge to $\mathbf{v}$ and $\mathbf{u}$ for $l \to \infty$. We define

$$\mathbf{F}^{(l)} := I + \nabla \mathbf{v}^{(l)}, \quad J^{(l)} := \det \mathbf{F}^{(l)}$$

and solve the sequence of linearized systems

$$\begin{aligned}
\left(\rho_f J^{(l-1)} \left(k^{-1}(\mathbf{v}^{(l)} - \mathbf{v}^{\text{old}}) + \right.\right. \\
+\mathbf{F}^{(l-1)^{-1}}(\mathbf{v}^{(l-1)} - k^{-1}(\mathbf{u}^{(l-1)} - \mathbf{u}^{\text{old}})) \cdot \nabla \mathbf{v}^{(l)}\Big), \phi\Big)_{\mathcal{F}} \\
+\left(J^{(l-1)} \boldsymbol{\sigma}_f(\mathbf{v}^{(l)}, p^{(l)}) \mathbf{F}^{(l-1)^{-T}}, \nabla\phi\right)_{\mathcal{F}} = (J^{(l-1)} \rho_f \mathbf{f}, \phi)_{\mathcal{F}} \\
\left(J^{(l-1)} \mathbf{F}^{(l-1)^{-1}} : \nabla \mathbf{v}^T, \xi\right)_{\mathcal{F}} = 0 \\
(\rho_s^0 k^{-1}(\mathbf{v}^{(l)} - \mathbf{v}^{\text{old}}), \phi)_{\mathcal{S}} + (\mathbf{F}^{(l-1)} \boldsymbol{\Sigma}_s^{(l)}, \nabla\phi)_{\mathcal{S}} = (\rho_s^0 \mathbf{f}, \phi)_{\mathcal{S}} \\
(k^{-1}(\mathbf{u}^{(l)} - \mathbf{u}^{\text{old}}) - \mathbf{v}^{(l)}, \psi_s)_{\mathcal{S}} = 0 \\
(\nabla \mathbf{u}^{(l)}, \nabla \psi_f)_{\mathcal{F}} = 0,
\end{aligned} \tag{5.7}$$

with an ad hoc linearization of the solid's stress tensor (here, given for the St. Venant Kirchhoff material)

$$\begin{aligned}
\boldsymbol{\Sigma}_s^{(l)} &:= 2\mu_s \mathbf{E}_s^{(l)} + \lambda_s \operatorname{tr}(\mathbf{E}_s^{(l)}) I, \\
\mathbf{E}_s^{(l)} &:= \frac{1}{2}\left(\nabla \mathbf{u}^{(l)} + \nabla \mathbf{u}^{(l)^T} + \nabla \mathbf{u}^{(l-1)} \nabla \mathbf{u}^{(l)^T}\right).
\end{aligned}$$

Other choices are possible. This fixed-point linearization of the fsi system is similar to the Oseen linearization of the Navier-Stokes system, see Sect. 4.4.1. A theoretical analysis on the convergence of this fixed-point iteration is difficult, but we will add numerical tests using the benchmark problem fsi-3 of Hron and Turek [199], see Sect. 5.2.3.

5.2.2 *Newton Linearization for Fluid-structure Interactions in Arbitrary Lagrangian Eulerian Formulation*

In Sect. 4.4, we have seen that general fixed-point iterations for the linearization of the Navier-Stokes system usually show very slow convergence properties, see Fig. 4.9. Only by using Newton scheme for approximation of the nonlinear systems, we could establish a robust and very fast converging scheme. This section will now describe Newton linearization for fluid-structure interactions in ALE formulation. The main difficulty will again be the handling of the domain motion, hidden in the ALE mapping T, its gradient $\mathbf{F}$ and determinant J. By consulting Sect. 4.4.2, the general Newton method for a (quasi-)stationary system of partial differential equations in variational formulation was given as (compare (4.34))

$$\mathbf{W} \in \mathcal{X}: \quad A'(\mathbf{U}^{(l-1)})(\mathbf{W}^{(l)}, \Phi) = F(\Phi) - A(\mathbf{U}^{(l-1)})(\Phi), \quad \forall \Phi \in \mathcal{Y}, \tag{5.8}$$

with

$$\mathbf{U}^{(l)} := \mathbf{U}^{(l-1)} + \omega^{(l)}\mathbf{W}^{(l)}. \tag{5.9}$$

In the context of fluid-structure interactions in ALE formulation (discretized in time with the backward Euler method) the last known approximation $\mathbf{U}^{(l-1)} \in \mathcal{X}$ is given by

$$\mathbf{U}^{(l-1)} := \{\mathbf{v}^{(l-1)}, \mathbf{u}^{(l-1)}, p_f^{(l-1)}\} \in \mathcal{X} = \mathcal{V} \times \mathcal{W} \times \mathcal{L}_f.$$

We denote the unknown update by

$$\mathbf{W}^{(l)} = \{\mathbf{z}, \mathbf{w}, q_f\} \in \mathcal{X} = \mathcal{V} \times \mathcal{W} \times \mathcal{L}_f.$$

Remark 5.1 (Initial Value) Newton convergence highly depends on a good choice of an initial approximation $\mathbf{U}^{(0)}$. In the context of non-stationary problems, a good choice is always to use the old solution at time t_{n-1}, hence $\mathbf{U}^{(0)} = \mathbf{U}(t_{n-1}) = \mathbf{U}^{\text{old}}$. This initial choice could even be enhanced by using a linear extrapolation of the two last approximations, by choosing

$$\mathbf{U}^{(0)} = \mathbf{U}(t_{n-1}) + \frac{t_n - t_{n-1}}{t_{n-1} - t_{n-2}} \left(\mathbf{U}(t_{n-1}) - \mathbf{U}(t_{n-2})\right).$$

Considering the backward Euler discretization, the semilinear form $A(\cdot)(\cdot)$ is given by (compare 5.5)

$$\begin{aligned} A(\mathbf{U})(\Phi) = &\left(\rho_f J \left(k^{-1}(\mathbf{v} - \mathbf{v}^{\text{old}}) + \nabla\mathbf{v}\mathbf{F}^{-1}\left(\mathbf{v} - k^{-1}(\mathbf{u} - \mathbf{u}^{\text{old}})\right)\right), \phi\right)_{\mathcal{F}} \\ &+ \left(J\boldsymbol{\sigma}_f\mathbf{F}^{-T}, \nabla\phi\right)_{\mathcal{F}} - (J\rho_f\mathbf{f}, \phi)_{\mathcal{F}} \\ &+ \left(J\mathbf{F}^{-1} : \nabla\mathbf{v}^T, \xi\right)_{\mathcal{F}} \\ &+ (\rho_s^0 k^{-1}\mathbf{v}, \phi)_{\mathcal{S}} + (\mathbf{F}\boldsymbol{\Sigma}_s, \nabla\phi)_{\mathcal{S}} \\ &+ (k^{-1}\mathbf{u} - \mathbf{v}, \psi_s)_{\mathcal{S}} + (\nabla\mathbf{u}, \nabla\psi_f)_{\mathcal{F}} \end{aligned} \tag{5.10}$$

and the right hand side $F(\cdot)$ by

$$F(\Phi) = (\rho_s^0\mathbf{f}, \phi)_{\mathcal{S}} + (\rho_s^0 k^{-1}\mathbf{v}^{\text{old}}, \phi)_{\mathcal{S}} + (k^{-1}\mathbf{u}^{\text{old}}\psi_s)_{\mathcal{S}}. \tag{5.11}$$

To simplify the representation of the derivatives of the convective term, we have—in (5.10)—used the relation

$$\left((\mathbf{F}^{-1}\mathbf{v}) \cdot \nabla\right)\mathbf{w} = \nabla\mathbf{v}\mathbf{F}^{-1}\mathbf{w}.$$

The data term $(J\rho_f \mathbf{f}, \phi)_{\mathcal{F}}$ must reside in the form $A(\cdot)(\cdot)$ as the deformation determinant J depends on the unknown deformation $\mathbf{u}$. The same applies to the old solution $\mathbf{v}^{\text{old}}$ appearing in the momentum equation of the fluid problem.

The derivative $A'(\mathbf{U}^{(l-1)})(\mathbf{W}^{(l)}, \Phi)$ in (5.8) is the Gâteaux derivative of the semilinear form $A(\cdot)(\cdot)$, which is the directional derivative at $\mathbf{U}^{(l-1)}$ in direction $\mathbf{W}^{(l)}$ tested with Φ. It is defined as

$$A'(\mathbf{U})(\mathbf{W}, \Phi) := \lim_{s\to 0} \frac{d}{ds} A(\mathbf{U} + s\mathbf{W})(\Phi)\Big|_{s=0}. \tag{5.12}$$

On a fixed domain, we can exchange the order of differentiation and integration, such that it holds

$$\frac{d}{ds}\left(\int_\Omega f(\mathbf{u} + s\mathbf{w})\phi \,\mathrm{d}x\right)\Big|_{s=0} = \int_\Omega \frac{d}{ds} f(\mathbf{u} + s\mathbf{w})\Big|_{s=0} \phi \,\mathrm{d}x.$$

Hence,

$$\frac{d}{ds}\left(f(\mathbf{u} + s\mathbf{w}), \phi\right)_\Omega \Big|_{s=0} = \left(f'(\mathbf{u})\mathbf{w}, \phi\right)_\Omega.$$

In the case of fluid-structure interaction, this situation is more involved, as the motion of the domain depends on the solution. Formally, variational formulations of fluid-structure interactions are defined on domains that depend on the solution. Here, differentiation and integration may not be exchanged

$$\frac{d}{ds}\left(f(\mathbf{u} + s\mathbf{w}), \phi\right)_{\Omega(\mathbf{u})} \Big|_{s=0} \neq \left(f'(\mathbf{u})\mathbf{w}, \phi\right)_{\Omega(\mathbf{u})}.$$

Instead, the derivative with respect to the domain of integration must be considered.

A straightforward and simple way for computing the derivative $A'(\cdot)(\cdot,\cdot)$ is by means of finite differences:

$$A'(\mathbf{U})(\mathbf{W}, \Phi) = \varepsilon^{-1}\left(A(\mathbf{U} + \varepsilon\mathbf{W})(\Phi) - A(\mathbf{U})(\Phi)\right) + \mathcal{O}(\varepsilon), \quad \varepsilon > 0 \tag{5.13}$$

This approach is widely used for complex simulations [170]. The main difficulty of finite difference approximations is the choice of ε. This parameter must be small enough, such that the approximation accuracy of the Jacobian (5.13) is high. On the other hand, a too small value of ε may cause cancellation effects and will give rise to a substantial truncation error. An optimal choice based on a priori information is usually not possible, see [47] where the authors investigated finite difference approximations in the context of gradient based optimization.

If the derivatives (5.12) are to be evaluated exactly, we need to manage the domain deformation. It will turn out, that our strict form of the *Arbitrary Lagrangian Eulerian* framework that works on a fixed reference system for the complete variational form, see (5.10) and (5.11), helps to avoid all difficulties, as

the computational domains are fixed. We can exchange orders of differentiation and integration. Using the alternative formulation on updated meshes, motion of the domains must be carefully included. Fernandez and Moubachir [141] use the concept of shape derivatives to include the mesh motion. They derive the exact analytical Jacobian for the fluid-structure interaction system in a very similar fashion to the present approach. Van der Zee and co workers [358, 359] describe two different approaches for differentiation of the variational formulation. The first approach [358] is very similar to our strict interpretation of the ALE method: the equations are mapped to the fixed reference domain, and all differentiation is carried out here. The second approach [359] is based on the theory of *shape calculus*, see [313, 362], where the derivative with respect to the domain motion is explicitly computed: let $T(t) : \Omega \to \Omega(t)$ be a sufficiently regular domain map. Then, the following fundamental formula holds:

$$\frac{d}{ds}\int_{\Omega(s)} f(x)\mathrm{d}x = \int_{\partial\Omega(s)} \langle \mathbf{n}\cdot\partial_s T(s)\rangle f(o)\mathrm{d}o,$$

where $\mathbf{n}$ is the outward facing unit normal at the boundary of $\Omega(s)$. We will have to get back to this approach, when dealing with the Fully Eulerian approach in Sect. 6.4. Here, we can rely on the strict variant of the ALE method, where all domains are fixed.

The following theorem gives the full Jacobian of the fluid-structure interaction problem in ALE coordinates, discretized with the backward Euler equation.

Theorem 5.2 (Jacobian for Fluid-structure Interactions in Arbitrary Lagrangian Eulerian Coordinates) *Let* $\mathbf{U} = \{\mathbf{v}, \mathbf{u}, p_f\} \in \mathcal{X}$, $\mathbf{W} = \{\mathbf{z}, \mathbf{w}, q_f\} \in \mathcal{X}$ *and* $\Phi = \{\phi, \psi_f, \psi_s, \xi_f\} \in \mathcal{Y}$. *For the directional derivative of (5.10) at* $\mathbf{U}$ *in direction of* $\mathbf{W}$, *it holds:*

$$\begin{aligned}
A'(\mathbf{U})(\mathbf{W}\,,\,\Phi) = &\left(\rho_f J\left(k^{-1}\mathbf{z} + \nabla\mathbf{z}\mathbf{F}^{-1}\left(\mathbf{v} - \frac{\mathbf{u}-\mathbf{u}^{old}}{k}\right) + \nabla\mathbf{v}\mathbf{F}^{-1}\mathbf{z}\right), \phi\right)_{\mathcal{F}} \\
&+ \left(J\frac{d\boldsymbol{\sigma}_f}{d\mathbf{v}}(\mathbf{W})\mathbf{F}^{-T}, \nabla\phi\right)_{\mathcal{F}} - \left(J\mathbf{F}^{-T}q_f, \nabla\phi\right)_{\mathcal{F}} \\
&+ \left((J\mathbf{F}^{-1} : \nabla\mathbf{z}^T, \xi\right)_{\mathcal{F}} \\
&+ \Big(\rho_f J\,\mathrm{tr}\,(\mathbf{F}^{-1}\nabla\mathbf{w})\Big(k^{-1}(\mathbf{v}-\mathbf{v}^{old}) + \\
&\quad \nabla\mathbf{v}\mathbf{F}^{-1}\left(\mathbf{v} - k^{-1}(\mathbf{u}-\mathbf{u}^{old})\right)\Big), \phi\Big)_{\mathcal{F}} \\
&- \left(\rho_f J\nabla\mathbf{v}\mathbf{F}^{-1}\nabla\mathbf{w}\mathbf{F}^{-1}\left(\mathbf{v} - k^{-1}(\mathbf{u}-\mathbf{u}^{old})\right), \phi\right)_{\mathcal{F}} \\
&- \left(\rho_f J\nabla\mathbf{v}\mathbf{F}^{-1}k^{-1}\mathbf{w}, \phi\right)_{\mathcal{F}} \\
&+ \left(J\,\mathrm{tr}\,(\mathbf{F}^{-1}\nabla\mathbf{w})\boldsymbol{\sigma}_f\mathbf{F}^{-T}, \nabla\phi\right)_{\mathcal{F}} - \left(J\boldsymbol{\sigma}_f\mathbf{F}^{-T}\nabla\mathbf{w}^T\mathbf{F}^{-T}, \nabla\phi\right)_{\mathcal{F}}
\end{aligned}$$

$$
\begin{aligned}
&+\left(J\frac{d\boldsymbol{\sigma}_f}{d\mathbf{u}}(\mathbf{W})\mathbf{F}^{-T},\nabla\phi\right)_{\mathcal{F}}\\
&+\left(J(\mathbf{F}^{-T}:\nabla\mathbf{w})(\mathbf{F}^{-1}:\nabla\mathbf{v}^T),\xi\right)_{\mathcal{F}}-\left(J\mathbf{F}^{-1}\nabla\mathbf{w}\mathbf{F}^{-1}:\nabla\mathbf{v}^T,\xi\right)_{\mathcal{F}}\\
&+\left(\rho_s^0k^{-1}\mathbf{z},\phi\right)_{\mathcal{S}}+\left(\nabla\mathbf{w}\boldsymbol{\Sigma}_s+\mathbf{F}\frac{d\boldsymbol{\Sigma}_s}{d\mathbf{u}}(\mathbf{W}),\nabla\phi\right)_{\mathcal{S}}\\
&-(\mathbf{z},\psi_s)_{\mathcal{S}}+(k^{-1}\mathbf{w},\psi_s)_{\mathcal{S}}\\
&+\left(\nabla\mathbf{w},\nabla\psi_f\right)_{\mathcal{F}},
\end{aligned}
\tag{5.14}
$$

where the directional derivatives of the Navier-Stokes stress tensor are given by

$$
\begin{aligned}
\frac{d}{d\mathbf{v}}\boldsymbol{\sigma}_f(\mathbf{U})(\mathbf{z})&=\rho_f\nu_f(\nabla\mathbf{z}_f\mathbf{F}^{-1}+\mathbf{F}^{-T}\nabla\mathbf{z}_f^T),\\
\frac{d}{d\mathbf{u}}\boldsymbol{\sigma}_f(\mathbf{U})(\mathbf{w})&=-\rho_f\nu_f\left(\nabla\mathbf{v}\mathbf{F}^{-1}\nabla\mathbf{w}\mathbf{F}^{-1}+\mathbf{F}^{-T}\nabla\mathbf{w}^T\mathbf{F}^{-T}\nabla\mathbf{v}^T\right),
\end{aligned}
$$

and where the directional derivatives of the St. Venant Kirchhoff material's tensor are given by

$$
\begin{aligned}
\frac{d\boldsymbol{\Sigma}_s}{d\mathbf{u}}(\mathbf{U})(\mathbf{w})&=2\mu_s\frac{d\mathbf{E}_s}{d\mathbf{u}}(\mathbf{W})+\lambda_s\,\mathrm{tr}\left(\frac{d\mathbf{E}_s}{d\mathbf{u}}(\mathbf{W})\right),\\
\frac{d\mathbf{E}_s}{d\mathbf{u}}(\mathbf{W})&=\frac{1}{2}(\nabla\mathbf{w}^T\mathbf{F}+\mathbf{F}^T\nabla\mathbf{w})
\end{aligned}
$$

Proof The proof is split into different part by a partitioning of the semilinear form (5.10) into subparts for Navier-Stokes momentum equation

$$
\begin{aligned}
A^{m,f}(\mathbf{U})(\Phi)=&\left(\rho_fJ\left(k^{-1}(\mathbf{v}-\mathbf{v}^{\mathrm{old}})+\mathbf{F}^{-1}(\mathbf{v}-k^{-1}(\mathbf{u}-\mathbf{u}^{\mathrm{old}}))\cdot\nabla\mathbf{v}\right),\phi\right)_{\mathcal{F}}\\
&+\left(J\boldsymbol{\sigma}_f\mathbf{F}^{-T},\nabla\phi\right)_{\mathcal{F}}-(J\rho_f\mathbf{f},\phi)_{\mathcal{F}},
\end{aligned}
\tag{5.15}
$$

the equation for divergence freeness

$$
A^{div,f}(\mathbf{U})(\Phi)=\left(J\mathbf{F}^{-1}:\nabla\mathbf{v}^T,\xi_f\right)_{\mathcal{F}},
\tag{5.16}
$$

the momentum equation of the solid problem and the velocity deformation relation

$$
\begin{aligned}
A^{m,s}(\mathbf{U})(\Phi)&=(\rho_s^0k^{-1}\mathbf{v},\phi)_{\mathcal{S}}+(\mathbf{F}\boldsymbol{\Sigma}_s,\nabla\phi)_{\mathcal{S}},\\
A^{uv,s}(\mathbf{U})(\Phi)&=(k^{-1}\mathbf{u}-\mathbf{v},\psi_s)_{\mathcal{S}},
\end{aligned}
\tag{5.17}
$$

and finally the (harmonic) extension of the deformation that defines the ALE mapping

$$A^{ale,f}(\mathbf{U})(\Phi) = (\nabla \mathbf{u}, \nabla \psi_f)_{\mathcal{F}}. \tag{5.18}$$

The full variational form $A(\mathbf{U})(\Phi)$ is given as the sum of $A^{m,f}(\mathbf{U})(\Phi) + A^{div,f}(\mathbf{U})(\Phi) + A^{m,s}(\mathbf{U})(\Phi) + A^{uv,s}(\mathbf{U})(\Phi) + A^{ale,f}(\mathbf{U})(\Phi)$.

Calculation of the different derivatives of these forms with respect to $\mathbf{v}$, $\mathbf{u}$ and p_f is done in the following lemmas. First, in Lemma 5.3 we deal with the derivatives of $A^{NS}(\cdot)(\cdot)$ and $A^{div}(\cdot)(\cdot)$ (the Navier-Stokes part). The Jacobian for the harmonic ALE extension (a linear operator) is easily available. Then, Lemma 5.5 shows the directional derivatives of the structure equation. And finally, Lemma 5.6 takes care of the derivatives of the Navier-Stokes part with respect to the artificial domain motion. This part only comes from the ALE formulation and would not be present in Eulerian formulations of the Navier-Stokes problem. □

Lemma 5.3 (Derivatives of the Navier-Stokes Equations with Respect to Velocity and Pressure) *For the directional derivatives of $A^{m,f}$ and $A^{div,f}$ in direction of velocity $\mathbf{v}$ and pressure p_f it holds*

$$\begin{aligned}
A^{m,f}_{\mathbf{v}}(\mathbf{U})(\mathbf{W}, \Phi) &= \left(\rho_f J k^{-1}\mathbf{z}, \phi\right)_{\mathcal{F}} \\
&\quad + \left(\rho_f J \left(\nabla \mathbf{z}\mathbf{F}^{-1}\left(\mathbf{v} - \frac{\mathbf{u} - \mathbf{u}^{old}}{k}\right) + \nabla \mathbf{v}\mathbf{F}^{-1}\mathbf{z}\right), \phi\right)_{\mathcal{F}} \\
&\quad + \left(J\frac{d\boldsymbol{\sigma}_f}{d\mathbf{v}}(\mathbf{W})\mathbf{F}^{-T}, \nabla\phi\right)_{\mathcal{F}}, \\
A^{m,f}_{p_f}(\mathbf{U})(\mathbf{W}, \Phi) &= -\left(J\mathbf{F}^{-T} q_f, \nabla\phi\right)_{\mathcal{F}}, \\
A^{div,f}_{\mathbf{v}}(\mathbf{U})(\mathbf{W}, \Phi) &= \left(J\mathbf{F}^{-1} : \nabla \mathbf{z}^T, \xi_f\right)_{\mathcal{F}}.
\end{aligned}$$

The derivative of the fluid's stress tensor is given by

$$\frac{d\boldsymbol{\sigma}_f}{d\mathbf{v}}(\mathbf{W}) = \rho_f \nu_f (\nabla \mathbf{z}_f \mathbf{F}^{-1} + \mathbf{F}^{T} \nabla \mathbf{z}_f^T).$$

Proof By the definition of the Gâteaux derivative (5.12), calculation of the derivatives is given by standard scalar differentiation, as the order of integration and differentiation can be exchanged. For the derivatives of the stress tensor, consult its ALE form (5.6). For basics on the linearization of the Navier-Stokes equations, see Sect. 4.4.2. □

Before proceeding with the St. Venant Kirchhoff material and the derivatives of the ALE formulation with respect to the deformation, we gather some useful relations.

Lemma 5.4 (Derivatives of the Deformation Gradient) *Let* $\mathbf{F} := I + \nabla \mathbf{u}$ *and* $J := \det \mathbf{F}$ *its gradient. It holds*

$$
\begin{aligned}
(i) \quad & \frac{d\mathbf{F}}{d\mathbf{u}}(\mathbf{w}) = \nabla \mathbf{w}, \\
(ii) \quad & \frac{d\mathbf{F}^T}{d\mathbf{u}}(\mathbf{w}) = \nabla \mathbf{w}^T, \\
(iii) \quad & \frac{d\mathbf{F}^{-1}}{d\mathbf{u}}(\mathbf{w}) = -\mathbf{F}^{-1} \nabla \mathbf{w} \mathbf{F}^{-1}, \\
(iv) \quad & \frac{d\mathbf{F}^{-T}}{d\mathbf{u}}(\mathbf{w}) = -\mathbf{F}^{-T} \nabla \mathbf{w}^T \mathbf{F}^{-T}, \\
(v) \quad & \frac{dJ}{d\mathbf{u}}(\mathbf{w}) = J\mathbf{F}^{-T} : \nabla \mathbf{w} = J \operatorname{tr}(\mathbf{F}^{-1} \nabla \mathbf{w})
\end{aligned}
$$

Proof Relations *(i)* and *(ii)* are directly available. For showing relation *(iii)* we differentiate the identity $\mathbf{F}^{-1}\mathbf{F} = I$ and use *(i)* to obtain

$$
\frac{d}{d\mathbf{u}} \left(\mathbf{F}^{-1}\mathbf{F} \right)(\mathbf{w}) = \frac{d}{d\mathbf{u}} I(\mathbf{w}) = 0 \quad \Rightarrow \quad \frac{d\mathbf{F}^{-1}}{d\mathbf{u}}(\mathbf{w})\mathbf{F} + \mathbf{F}^{-1} \frac{d\mathbf{F}}{d\mathbf{u}}(\mathbf{w}) = 0.
$$

Multiplication with $\mathbf{F}^{-1}$ gives the result:

$$
\frac{d\mathbf{F}^{-1}}{d\mathbf{u}}(\mathbf{w}) = -\mathbf{F}^{-1} \nabla \mathbf{w} \mathbf{F}^{-1}.
$$

(iv) is the transpose of *(iii)*. Relation *(v)* can be shown by component-wise calculation. □

With Lemma 5.4, we can now compute the Jacobian of the elastic structure equations with respect to velocity and deformation:

Lemma 5.5 (Derivative of the Structure Equation with Respect to Velocity and Deformation) *It holds for the derivatives of the elastic structure equation in reference coordinates with respect to velocity and deformation:*

$$
\begin{aligned}
A_{\mathbf{v}}^{m,s}(\mathbf{U})(\mathbf{W}, \Phi) &= \left(\rho_s^0 k^{-1} \mathbf{z}, \phi \right)_{\mathcal{S}} \\
A_{\mathbf{u}}^{m,s}(\mathbf{U})(\mathbf{W}, \Phi) &= \left(\nabla \mathbf{w} \boldsymbol{\Sigma}_s + \mathbf{F} \frac{d\boldsymbol{\Sigma}_s}{d\mathbf{u}}(\mathbf{W}), \nabla \phi \right)_{\mathcal{S}}, \\
A_{\mathbf{v}}^{uv,s}(\mathbf{U})(\mathbf{W}, \Phi) &= -(\mathbf{z}, \psi_s)_{\mathcal{S}}, \\
A_{\mathbf{u}}^{uv,s}(\mathbf{U})(\mathbf{W}, \Phi) &= (k^{-1}\mathbf{w}, \psi_s)_{\mathcal{S}},
\end{aligned}
$$

where the derivative of the 2nd Piola Kirchhoff stress tensor $\boldsymbol{\Sigma}_s$ (of the St. Venant Kirchhoff material) is given by

$$\frac{d\boldsymbol{\Sigma}_s}{d\mathbf{u}}(\mathbf{W}) = 2\mu_s \frac{d\mathbf{E}_s}{d\mathbf{u}}(\mathbf{W}) + \lambda_s \operatorname{tr}\left(\frac{d\mathbf{E}_s}{d\mathbf{u}}(\mathbf{W})\right),$$

and the derivative of the Green-Lagrangian strain tensor $\mathbf{E}_s$ by

$$\frac{d\mathbf{E}_s}{d\mathbf{u}}(\mathbf{W}) = \frac{1}{2}(\nabla \mathbf{w}^T \mathbf{F} + \mathbf{F}^T \nabla \mathbf{w}).$$

Proof These relations follow using *(i)* and *(ii)* of Lemma 5.4. □.

Finally, it remains to gather all derivatives with respect to the ALE domain mapping. Omitting some of the derivatives (which here correspond to the dependency of the domain motion) relates to a simplified Newton method, see Sect. 5.2.3 for a numerical study.

Lemma 5.6 (Derivative of the Navier-Stokes Equations with Respect to the Domain Motion) *It holds for the derivatives of the Navier-Stokes equations in ALE coordinates with respect to the domain motion u*

$$\begin{aligned}
A_{\mathbf{u}}^{m,f}(\mathbf{U})(\mathbf{W}, \Phi) = &\left(\rho_f \operatorname{tr}(\mathbf{F}^{-1}\nabla \mathbf{w})\left(k^{-1}(\mathbf{v} - \mathbf{v}^{old}) + \right.\right. \\
&\left.\left. \nabla \mathbf{v}\mathbf{F}^{-1}\left(\mathbf{v} - k^{-1}(\mathbf{u} - \mathbf{u}^{old})\right)\right), \phi\right)_{\mathcal{F}} \\
&- \left(\rho_f J \nabla \mathbf{v}\mathbf{F}^{-1}\nabla \mathbf{w}\mathbf{F}^{-1}\left(\mathbf{v} - k^{-1}(\mathbf{u} - \mathbf{u}^{old})\right), \phi\right)_{\mathcal{F}} \\
&- \left(\rho_f J \nabla \mathbf{v}\mathbf{F}^{-1}k^{-1}\mathbf{w}, \phi\right)_{\mathcal{F}} \\
&+ \left(\operatorname{tr}(\mathbf{F}^{-1}\nabla \mathbf{w})\boldsymbol{\sigma}_f \mathbf{F}^{-T}, \nabla \phi\right)_{\mathcal{F}} - \left(J\boldsymbol{\sigma}_f \mathbf{F}^{-T}\nabla \mathbf{w}^T \mathbf{F}^{-T}, \nabla \phi\right)_{\mathcal{F}} \\
&+ \left(J\frac{d\boldsymbol{\sigma}_f}{d\mathbf{u}}(\mathbf{W})\mathbf{F}^{-T}, \nabla \phi\right)_{\mathcal{F}}, \\
A_{\mathbf{u}}^{div,f}(\mathbf{U})(\mathbf{W}, \Phi) = &\left(\operatorname{div}\left(\operatorname{tr}(\mathbf{F}^{-1}\nabla \mathbf{w})\mathbf{F}^{-1}\mathbf{v}\right), \xi_f\right)_{\mathcal{F}} \\
&- \left(\operatorname{div}\left(J\mathbf{F}^{-1}\nabla \mathbf{w}\mathbf{F}^{-1}\right), \xi_f\right)_{\mathcal{F}}.
\end{aligned}$$

where the derivative of the stress tensor with respect to the domain motion is given by

$$\frac{d\boldsymbol{\sigma}_f}{d\mathbf{u}}(\mathbf{W}) = -\rho_f \nu_f \left(\nabla \mathbf{v}\mathbf{F}^{-1}\nabla \mathbf{w}\mathbf{F}^{-1} + \mathbf{F}^{-T}\nabla \mathbf{w}^T \mathbf{F}^{-T}\nabla \mathbf{v}^T\right)$$

Proof Again, all these derivatives can be estimated by tedious calculations and frequent use of Lemma 5.4. □

Further details on the computation of the Jacobian are given in [280], where the derivatives of the stationary fluid-structure interaction system are derived.

With the Jacobian of the fluid-structure interaction system at hand, we can formulate the linear systems of partial differential equations that define every step of the Newton approximation

$$A'(\mathbf{U}^{(l-1)})(\mathbf{W}^{(l)}, \Phi) = F(\Phi) - A(\mathbf{U}^{(l-1)})(\Phi) \quad \forall \Phi \in \mathcal{Y}. \tag{5.19}$$

The variational formulation defined by $A'(\cdot)(\cdot,\cdot)$ given in Theorem 5.2 is complex, it couples all different variables, but it is a linear problem. Finite element discretization of this problem will be subject to the following section. Later on, in Chap. 7, we will discuss the solution of the resulting (after discretization) linear systems of equations.

In every step of the Newton iteration, Eq. (5.19) is itself a coupled problem on the two domains $\mathcal{F}$ and $\mathcal{S}$. On the common interface, three coupling conditions are given. First, continuity of the velocity variation $\mathbf{z}$, second continuity of the deformation's variation $\mathbf{w}$ and finally, a Neumann condition that comes from the linearization of the dynamic coupling condition. For deriving its exact formulation, one would have to transform the Jacobian $A'(\mathbf{U})(\mathbf{W}, \Phi)$ back to the classical formulation.

A modern alternative to the analytical computation of the Jacobian is given by the idea of *automatic differentiation*, see Rall [264] and Griewank [171]. Automatic differentiation is an algorithmic approach that is based on the concept that every computer implementation, e.g. the implementation of the semilinear form $A(\cdot)(\cdot)$ will internally be split into a sequence of elementary mathematical operations (like multiplications, roots, basis functions like sine or cosine etc.). These elementary operations are then derived and set together using chain and product rule. Dunne [127] presents and implementation of a Newton method for fluid-structure interactions in ALE formulation based on automatic differentiation. In particular, if different complex models are studied, automatic differentiation will help to compute exact Jacobians in a fail-proof way. It will for instance be easy to implement complex and changing material laws. The concept of automatic differentiation is not to be confused with finite differences, where derivatives are only approximated.

Remark 5.7 (Inexact Newton Iteration) The assembly of the Jacobian is a very costly step within the Newton iteration. Considering the necessity to solve linear systems afterwards, a change of the Jacobian usually calls for additional work regarding the preparation of preconditioners in Krylov-Subspace iterations or smoothers in multigrid solvers, see Chap. 7. In the worst case, when direct solvers must be used to approximate the linear systems, a modification of the Jacobian also calls for a new decomposition of it. Hence, assembling the Jacobian must be prevented, whenever the overall efficiency does not require it. As linear systems are

usually only approximated up to a given tolerance, full quadratic convergence of the Newton method itself cannot be expected. Therefore, we only update the Jacobian, if the nonlinear convergence rate that can easily be measured as

$$\rho_n = \frac{\|F(\cdot) - A(\mathbf{U}^n)(\cdot)\|_\infty}{\|F(\cdot) - A(\mathbf{U}^{(n-1)})(\cdot)\|_\infty}, \tag{5.20}$$

is above a given threshold γ_{nt}. A good balance depends on the required tolerance and the efficiency of the linear solver. Usually, $\gamma_{nt} \approx 0.01 \sim 0.1$.

5.2.3 *Numerical Study on Linearizations*

We present a study on the linearization on the performance of different linearization techniques applied to the non-stationary benchmark problem fsi-3 introduced by Hron and Turek [200]. We have used this test case to study time discretizations in Sect. 5.1. Here we analyze the performance of the different choices for a linearization of the nonlinear problems. We investigate the time interval $I = [5, 5.5]$, where the oscillation is fully developed, such that significant deformations appear. This is important to account for the geometric nonlinearities that come from the ALE mapping, see Fig. 5.6.

All numerical studies are carried out with the implicitly shifted Crank-Nicolson scheme, see Sect. 4.1.2.1 with θ chosen as

$$\theta = \frac{1}{2} + 2k,$$

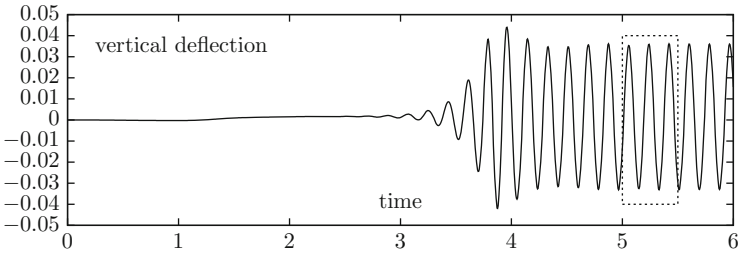

Fig. 5.6 Benchmark problem fsi-3. Vertical deflection of the tip of the beam as functional over time. We perform the numerical study on different linearization techniques in the sub-interval $I = [5, 5.5]$, where the dynamics of the flow is fully developed

where by k we denote the time step size. If not specified otherwise, we choose

$$k = 0.005,$$

such that a total of $N = 100$ steps is investigated and the effective parameter $\theta = 0.51$ is picked. For spatial discretization we choose equal-order biquadratic elements on a mesh with about 4000 unknowns.

In every time step, the nonlinear problems are approximated such that the initial residual is reduced by eight orders of magnitude

$$\|F(\cdot) - A(\mathbf{U}^n)(\cdot)\|_\infty \leq \text{tol}\|F(\cdot) - A(\mathbf{U}^0)(\cdot)\|_\infty, \quad \text{tol} = 10^{-8}.$$

The linear systems are solved by a direct method to prevent side-effects of not-sufficient accuracy.

In a first study, we compare the effects of the parameter γ_{nt} in (5.20), controlling the limiting reduction rate, where a new Jacobian is assembled. We choose the parameters

$$\gamma_{nt} \in \{0, 0.2, 0.5\},$$

where $\gamma_{nt} = 0$ corresponds to the exact Newton method with a new Jacobian in every step. Quadratic convergence should be reached.

In Fig. 5.7, we show the number of Newton steps required in every time step. Furthermore, we show the assembly-count of the Jacobian. Finally, we indicate the overall number of Jacobians and the overall computational time spend in the complete cycle $I = [5, 5.5]$.

All computations in this section are carried out on a Intel Xeon X5650 cpu using single core performance at 2.67 GHz. It can be seen that the number of Newton steps undergoes a certain periodicity. This is directly connected to the oscillation of the solution itself, see Fig. 5.6. Given a large deformation $\mathbf{u}$, the ALE-mapping has a significant nonlinear impact.

We observe that the number of required Newton steps increases, if the threshold γ_{nt} is enlarged. For the pure Newton scheme, a maximum of 7 steps is required, whereas for $\gamma_{nt} = 1$ a maximum of 15 steps is used. However, a smaller choice of γ_{nt} calls for a higher number of Jacobians to be assembled. For $\gamma_{nt} = 0$, a new Jacobian is assembled in every single step of the Newton iteration. Considering the computational time, this is a severe drawback as can be seen in the bottom plot of Fig. 5.7. Here, the cost for assembling matrix and setting up the decomposition for the direct solver is so high that the overall computational time is best for the choice $\gamma_{nt} = 0.5$. In the table below Fig. 5.7 we indicate the accumulated time for all time steps in the interval $I = [5, 5.5]$. Choosing $\gamma_{nt} = 0.2$ saves about 22% of

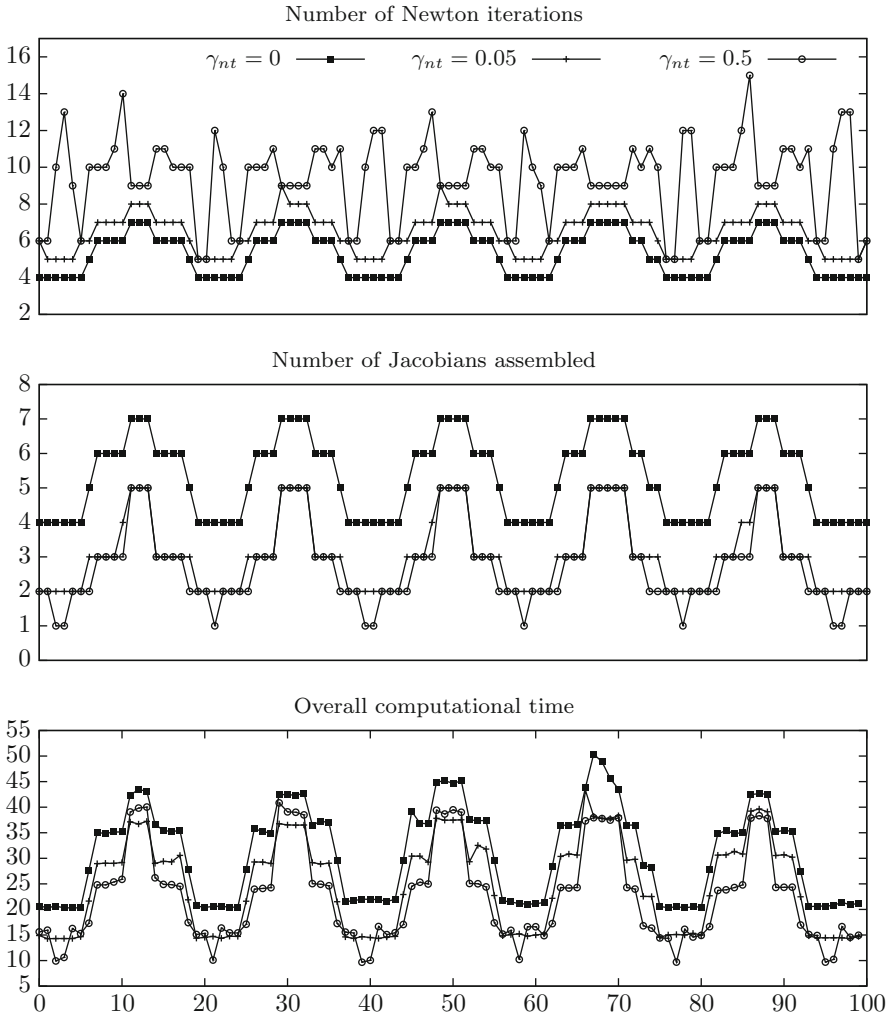

Matrix assembly tolerance γ_{nt}	0.0	0.2	0.5
Total Newton steps	532	777	938
Jacobians assembled	532	304	280
Total time (seconds)	3 099	2 388	2 250

Fig. 5.7 Comparison of the Newton iteration for different values of γ_{nt}, controlling the convergence-rate threshold, where a new Jacobian is assembled. The table shows the accumulated number of Newton steps, assemblies of the Jacobian and the total time (in seconds) for all 100 time steps

the computational time compared to $\gamma_{nt} = 0$ which corresponds to the full Newton method. The choice $\gamma_{nt} = 0.5$ increases the savings to 27%. This result however cannot be generalized, as a more efficient linear solver will have less overhead. Furthermore, increasing the effect of the nonlinearity, a too large value of γ_{nt} could severely increase the iteration count.

Next, in Fig. 5.8, we show the results for an approximation of the Jacobian by finite differences, i.e.

$$\frac{d}{ds}A(\mathbf{U} + s\mathbf{W})(\Phi)\Big|_{s=0} = \frac{A(\mathbf{U} + \varepsilon\mathbf{W})(\Phi) - A(\mathbf{U})(\Phi)}{\varepsilon} + \mathcal{O}(\varepsilon).$$

Approximation of the Jacobian by finite differences calls for multiple evaluations of the residual. First, we must compute

$$\mathcal{R}_0 = A(\mathbf{U})(\Phi),$$

then, we compute the directional derivatives with respect to the different components of velocity, deformation and pressure, i.e.

$$\mathcal{R}_{\mathbf{v}_i} = A(\mathbf{U} + \varepsilon\mathbf{z}_i)(\Phi), \quad \mathcal{R}_{\mathbf{u}_i} = A(\mathbf{U} + \varepsilon\mathbf{w}_i)(\Phi), \quad \mathcal{R}_p = A(\mathbf{U} + \varepsilon q)(\Phi),$$

for $i = 1, \ldots, d$. Altogether, 6 residual evaluations are required in 2d and 9 in 3d. By using a central difference approximation, this effort is even increased. The step size has to be chosen with care. For $\varepsilon = 10^{-6}$ we get a Newton-convergence that is comparable to the analytical evaluation of the Jacobian, see Fig. 5.8. However both for larger and smaller values of ε, the approximation quality worsens, such that a significant overhead appears. For $\varepsilon = 10^{-9}$, the approximation is governed by numerical cancellation effects. We have chosen $\gamma_{nt} = 0.2$ in all three cases. Comparing the summed values for the number of Newton steps and the number of Jacobian assemblies we see that the choice $\varepsilon = 10^{-6}$ leads to similar results compared to the table in Fig. 5.7 in the case $\gamma_{nt} = 0.2$. However, it turns out that using a finite difference approximation is more costly. Even if the Jacobian is so accurate that the Newton convergence is the same as in the case of an analytical Jacobian, the overall computational time is higher. If the finite difference parameter ε is not optimally chosen, the overall time can dramatically increase.

In Fig. 5.9 we directly compare the finite difference approximation to the analytical Jacobian. The number of Newton steps is about the same, the computational time for the difference approximation however is larger. This is due to the increased cost for the assembly of one single Jacobian. On a mesh with about 4000 unknowns, it took an average of about $t_J \approx 6.2\,\mathrm{s}$ to approximate the Jacobian with finite differences versus only $t_J \approx 1.5\,\mathrm{s}$, if the analytic derivation of the derivatives is used.

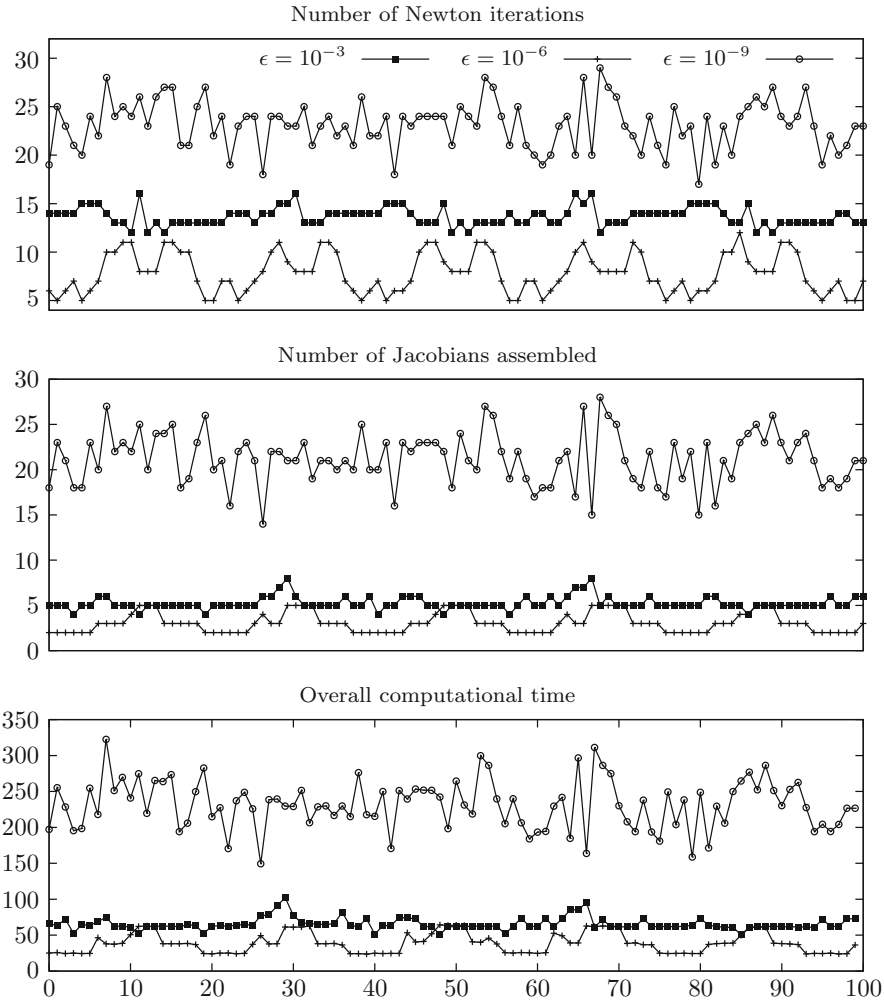

Finite difference parameter ε	10^{-3}	10^{-6}	10^{-9}
Total Newton steps	1 366	786	2 313
Jacobians assembled	525	307	2 121
Total time (seconds)	6 561	3 885	23 171

Fig. 5.8 Comparison of the Newton iteration with finite different approximation of the Jacobian $A'(\mathbf{U})(\Phi) \approx \varepsilon^{-1}(A(\mathbf{U} + \varepsilon\mathbf{W})(\Phi) - A(\mathbf{U})(\Phi))$. Different values of the step-size ε. The table shows the accumulated number of Newton steps, assemblies of the Jacobian and the total time (in seconds) for all 100 time steps

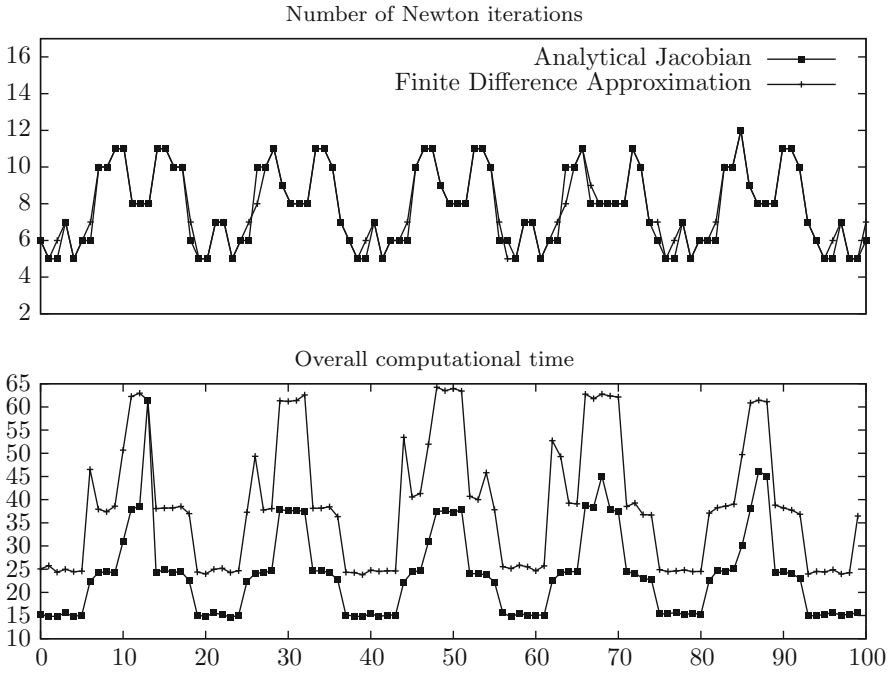

Fig. 5.9 Comparison of the Newton iteration with analytical and finite difference approximation of the Jacobian (using step-size $\varepsilon = 10^{-6}$)

We note that we used a direct solver for these calculations. On the present mesh, the time for decomposing the matrix is about 5 s in both cases, analytic evaluation and finite difference approximation.

Finally, we consider an inexact version of the Newton method, where the very costly derivatives with respect to the ALE mapping are neglected. In Fig. 5.10 we compare the Newton iteration considering a full Jacobian with the Newton iteration using the reduced Jacobian. We show the iteration count and the overall time spent in every Newton iteration. We observe that the reduced Jacobian yields a slightly larger iteration count. The overall time is reduced, as the assembly of each Jacobian takes only 1.25 s instead of 1.5 s for the full variant. Again we note that the effect would be stronger, if a more efficient linear solver is used.

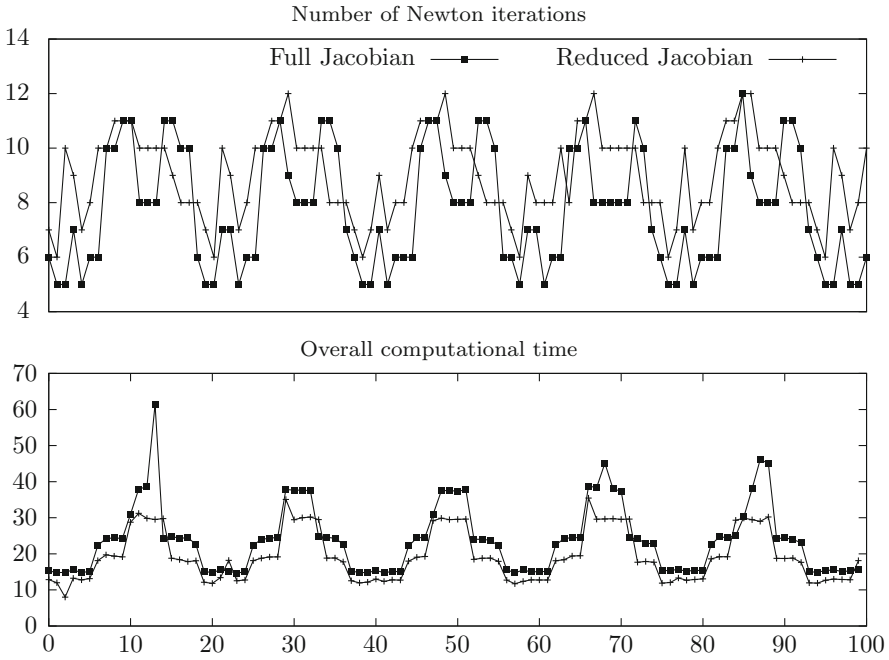

Jacobian approximation	full	approximated
Total Newton steps	777	902
Jacobians assembled	304	318
Total time (seconds)	2 388	1 937

Fig. 5.10 Comparison of the Newton iteration with full and reduced Jacobian. The table shows the accumulated number of Newton steps and Jacobian assembles as well as the computational time (in seconds) for all 100 time steps

5.3 Finite Elements for Fluid-structure Interactions in ALE Formulation

Every step of the Newton iteration requires the solution of a linear system of partial differential equations, compare (5.19)

$$\mathcal{W}^{(l)} := \{\mathbf{z}^{(l)}, \mathbf{w}^{(l)}, q_f^{(l)}\} \in \mathcal{X} := \mathcal{V} \times \mathcal{W} \times \mathcal{L}_f :$$
$$A'(\mathbf{U}^{(l-1)})(\mathbf{W}^{(l)}, \Phi) = G(\Phi)$$
$$\forall \Phi := \{\phi, \psi_f, \psi_s, \xi_f\} \in \mathcal{V} \times \mathcal{W}_f \times \mathcal{L}_s \times \mathcal{L}_f.$$

In the context of the backward Euler discretization of fluid-structure interactions on a fixed ALE domain, the bilinear-form $A'(\mathbf{U})(\cdot,\cdot)$ is given as in Theorem 5.2. The right hand side is given by

$$G(\Phi) := F(\Phi) - A(\mathbf{U}^{(l-1)})(\Phi),$$

where $\mathbf{U}^{(l-1)}$ is the last Newton approximation and $A(\mathbf{U}^{(l-1)})(\Phi)$ and $F(\Phi)$ are shown in (5.10) and (5.11). Trial spaces for velocity and deformation are defined on the whole domain

$$\mathcal{V} := H_0^1(\Omega;\Gamma^D)^d, \quad \mathcal{W} := H_0^1(\Omega;\partial\Omega)^d,$$

and differ in the choice of boundary values only. See Sect. 3.4 for a discussion.

The test function $\phi \in \mathcal{V}$ for both momentum equations is also defined on the complete domain Ω. All further test functions are defined sub-domain wise

$$\mathcal{L}_f := L^2(\mathcal{F}), \quad \mathcal{W}_f := H_0^1(\mathcal{F})^d, \quad \mathcal{L}_s := L^2(\mathcal{S})^d.$$

In the following, we will focus on the finite element discretization of these linear systems

$$\mathbf{W} \in \mathcal{X}: \quad A(\mathbf{W},\Phi) = G(\Phi) \quad \forall \Phi \in \mathcal{Y}, \tag{5.21}$$

where $A(\cdot,\cdot)$ is bilinear on $\mathcal{X}\times\mathcal{Y}$. Discretization is accomplished by restricting solution and test function to discrete spaces

$$\mathbf{W}_h \in X_h: \quad A(\mathbf{W}_h,\Phi_h) + S_h(\mathbf{W}_h,\Phi_h) = G(\Phi_h) \quad \forall \Phi \in Y_h, \tag{5.22}$$

where $S_h(\cdot,\cdot)$ defines some possible stabilization terms, see Sects. 4.3.2 and 4.4.3.

Remark 5.8 (Properties of Finite Element Spaces) For the choice of finite element spaces X_h and Y_h must consider the following properties

1. For a conforming (Petrov)-Galerkin formulation it must hold $X_h \subset \mathcal{X}$ and $Y_h \subset \mathcal{Y}$.
2. The dimension of test and trial spaces must coincide

$$\dim X_h = \dim Y_h.$$

3. The velocity- and pressure-coupling $\{\mathbf{v}_h, p_h\}$ within the fluid-domain must satisfy the inf-sup condition. Otherwise, the variational formulation has to be enriched by stabilization terms $S_h(\cdot,\cdot)$, see Sect. 4.3.2.
4. For implementation reasons, it is preferable to consider finite element spaces for velocity and deformation of the same type on $\mathcal{F}$ and $\mathcal{S}$.

5. As global velocity and deformation are continuous on the complete domain Ω, but not differentiable across the interface $\mathcal{I}$, it is preferable, if the interface is resolved by the triangulation. Otherwise, the order of convergence will be reduced, see Sect. 4.5, unless special manners are taken.

In the following we will discuss different choices of finite element triples for velocity, deformation and pressure. Besides conforming finite element spaces with continuous velocities and deformations the choice of discontinuous Galerkin methods is possible and also applied in the context of fluid-structure interactions, see Feistauer and coworkers [138].

5.3.1 Finite Element Triangulations for Fluid-structure Interactions in ALE Formulation

The benefit of the formulation in Arbitrary Lagrangian Eulerian coordinates is the fixation of the sub-domains $\mathcal{F}$ and $\mathcal{S}$, separated by the interface $\mathcal{I}$. We define:

Definition 5.9 (Matching Mesh) A triangulation Ω_h of the domain Ω is called a *matching mesh*, if for every element $K \in \Omega_h$ it holds

$$\Big(K \subset \mathcal{S} \ \wedge \ K \cap \mathcal{F} = \emptyset\Big) \vee \Big(K \subset \mathcal{F} \ \wedge \ K \cap \mathcal{S} = \emptyset\Big).$$

For a matching triangulation, we define the sub-triangulations

$$\Omega_{h,f} := \{K \in \Omega_h \mid K \subset \mathcal{F}\}, \quad \Omega_{h,s} := \{K \in \Omega_h \mid K \subset \mathcal{S}\}.$$

This definition implies that a matching mesh always resolves the interface $\mathcal{I}$ between fluid and solid by edges of elements, such that we can define

$$\mathcal{I}_h := \{e \in \partial K, \ K \in \Omega_h, \ e \in \mathcal{I}\},$$

and it holds

$$\bar{\mathcal{I}} = \bigcup_{e \in \mathcal{I}_h} \bar{e}.$$

This directly shows that matching meshes in this strict sense are only possible, if the interface $\mathcal{I}$ (in reference coordinates) is a polygonal, or if the interface can be described by low order polynomials, and if a parametric finite element triangulation is considered, see Definition 4.17. Here, we will always assume that all finite element meshes are matching.

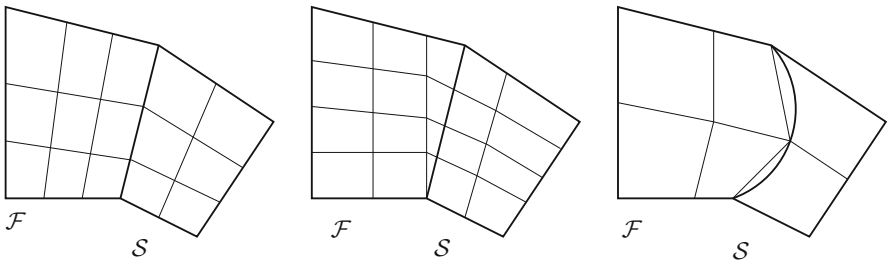

Fig. 5.11 Example of a matching mesh (*left*) and non-matching mesh (*middle*). The *right sketch* shows a generalized matching mesh at a curved interface. See Remark 5.10

Remark 5.10 (Approximation of Curved Interfaces) If the interface between fluid and solid is curved, such that it cannot be exactly resolved by the mesh, the strict definition of matching meshes is not applicable and will be relaxed: we will call a mesh matching, if all degrees of freedom used to define the parametric triangulation (see Definition 4.17) are either all part of the solid-domain $\bar{\mathcal{S}}$ or all part of the fluid-domain $\bar{\mathcal{F}}$. See Fig. 5.11 for examples of matching and non-matching triangulations.

In the finite element error analysis, the consideration of curved interfaces that cannot be resolved by the mesh (and hence not by the finite element spaces) is still an open problem.

It is not strictly required that one uses matching meshes for discretizing fluid-structure interactions. The use of matching meshes just simplifies the embedding of the coupling conditions, as we can define global function spaces V_h and W_h for velocity, deformation and the momentum equation's test function and restrict these global functions to the two sub-domains. By this approach, coupling will turn out to be as simple as in the continuous case, see Sect. 3.4.

Lemma 5.11 (Finite Elements Spaces on Matching Meshes) *Let Ω_h be a matching mesh of the domain Ω and V_h the standard space of continuous elements of degree $r \geq 1$ with Lagrangian basis $V_h = \text{span}\{\phi_h^{(i)},\ i = 1, \ldots, N\}$, e.g.*

$$\phi_h^{(i)}(x_j) = \delta_{ij},\ i, j \in \{1, \ldots, N\}.$$

See Sect. 4.2.1. The subspaces

$$V_{h,f} := \text{span}\{\phi_h^{(i)} \in V_h,\ x_i \in \bar{\mathcal{F}} \setminus \mathcal{I}\},$$
$$V_{h,s} := \text{span}\{\phi_h^{(i)} \in V_h,\ x_i \in \bar{\mathcal{S}}\},$$

define a division of V_h,

$$V_h = V_{h,f} + V_{h,s}, \quad \dim V_h = \dim V_{h,f} + \dim V_{h,s}. \tag{5.23}$$

The space $V_{h,f}$ is $H_0^1(\mathcal{F};\mathcal{I})$ conforming, the space $V_{h,s}$ is $H^1(\mathcal{S})$-conforming.

Proof For $\phi_h^{(i)}$ with $x_i \in \bar{\mathcal{F}}$, but $x_i \notin \mathcal{I}$, it holds on matching triangulations that

$$\text{supp } \phi_h^{(i)} \in \mathcal{F}.$$

Hence, $V_{h,f} \subset H_0^1(\mathcal{F};\mathcal{I})$. The relation $V_{h,s} \subset H^1(\mathcal{S})$ directly follows due to the continuity of $V_h \subset C(\bar{\Omega})$. Further, the dimension formula (5.23) follows, as the partitioning of Lagrange points $x_i \in \Omega_h$ to those on the interior of solid and fluid and those on the interface is unique. □

This lemma appears trivial, but it is essential for the following approach: if a global finite element function $\mathbf{v}_h \in V_h$ is given, we can define restrictions $\mathbf{v}_{h,f} \in V_{h,f}$ and $\mathbf{v}_{h,s} \in V_{h,s}$ in the two subspaces. This allows us to hide the coupling conditions in global trial and test spaces.

5.3.2 Inf-Sup Stable FE-Spaces for Fluid-structure Interactions in ALE Formulation

We will start by introducing some finite element triples (for velocity, deformation and pressure) that fulfill as many of the desirable properties from Remark 5.8. Let Ω_h be a matching triangulation. We will denote the velocity space by

$$\mathbf{v}_h \in V_h,$$

and the global deformation space by

$$\mathbf{u}_h \in W_h.$$

On the two sup-domains of the matching triangulation, we define the restrictions $\mathbf{v}_{h,f}, \mathbf{v}_{h,s}$ and $\mathbf{u}_{h,f}, \mathbf{u}_{h,s}$. We will denote the discrete pressure space by $L_{h,f}$.

As discussed in Sect. 4.3, the fluid's finite element pair for velocity $V_{h,f}$ and pressure $L_{h,f}$ must satisfy the inf-sup condition (in ALE coordinates):

$$\inf_{p_h \in L_{h,f}} \sup_{\mathbf{v}_h \in V_{h,f}} \frac{(p_h, \operatorname{div}(J_f \mathbf{F}_f^{-1} \mathbf{v}_h))_{\mathcal{F}}}{\|J_f^{\frac{1}{2}} p_h\|_{\mathcal{F}} \|J_f^{\frac{1}{2}} \nabla \mathbf{v}_h \mathbf{F}_f^{-T}\|_{\mathcal{F}}} \geq \hat{\gamma}_h. \tag{5.24}$$

where $\mathbf{F}_f$ and $J = \det \mathbf{F}_f$ come from the ALE-map. In terms of a computational finite element approach, the ALE-map is not a continuous, regular function, but itself defined by means of finite element functions

$$\mathbf{F}_h := I + \nabla \mathbf{u}_h, \quad J_h := \det \mathbf{F}_h.$$

In the following we will skip the index "h". The discussion of Sect. 2.5.2 has shown that the inf-sup condition in ALE formulation (5.24) is equivalent to the standard version of the inf-sup condition on the reference domains,

$$\inf_{p_h \in L_{h,f}} \sup_{\mathbf{v}_h \in V_{h,f}} \frac{(p_h, \operatorname{div} \mathbf{v}_h)_{\mathcal{F}}}{\|p_h\|_{\mathcal{F}} \|\nabla \mathbf{v}_h\|_{\mathcal{F}}} \geq \gamma, \tag{5.25}$$

if the domain mapping sufficiently regular. The two inf-sup constants however can significantly differ,

$$0 < \hat{\gamma} \ll \gamma,$$

if the deformation of the domain is large. An analysis of the inf-sup condition on transformed domains is given in [247]. By these considerations, we suggest the following choices of finite element triples for velocity, deformation and pressure. See also Fig. 5.12:

1. The generalized Taylor-Hood space

$$[Q^k]^d \times [Q^k]^d \times Q^{k-1}, \quad k \geq 2,$$

on quadrilateral meshes and

$$[P^2]^d \times [P^2]^d \times P^1, \quad [P^k]^d \times [P^k]^d \times P^{k-2}, \quad k \geq 3,$$

on triangular meshes. These spaces are inf-sup stable. Further, they have the simple property that deformation and velocity come from the same space. Finally, velocity and deformation spaces are the same on both parts of the domain.

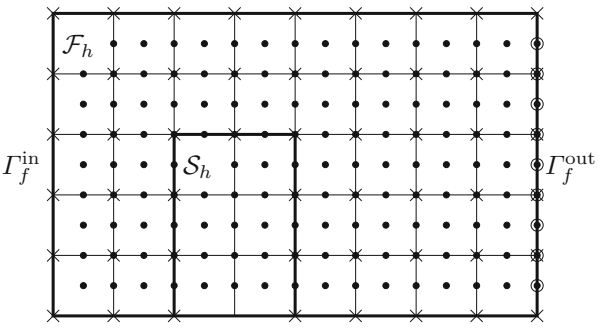

Fig. 5.12 The $Q^2-Q^2-Q^1$ finite element triple for velocity, deformation and pressure. By a *cross symbol* we denote pressure degrees of freedom and by *filled dot* degrees of freedom in velocity and deformation. By a *circled dot* we denote velocity degrees of freedom on the outflow boundary, where no deformation degree of freedom exists

2. The generalized Taylor-Hood spaces with discontinuous pressure

$$[Q^k]^d \times [Q^k]^d \times P^{k-1,dc}, \quad k \geq 2,$$

on quadrilateral meshes and the bulb-enriched space

$$[P^{2,bulb}]^d \times [P^2]^d \times P^{1,dc},$$

on triangular meshes. These two combinations have the same properties as the Taylor-Hood elements. Applications usually shows better solution quality (in particular on coarse meshes) due to local conservation properties that come from the use of discontinuous pressures.

Another advantage comes to the fore, if incompressible materials are considered, see Sect. 2.2.3. These material laws require the introduction of a second pressure variable $p_s \in L^2(\mathcal{S})$. As there is no physical reason for continuity of the two pressures p_f and p_s at the interface $\mathcal{I}$, the two discrete variables must be separated. Using continuous finite elements, this would cause technical problems, as there is only one Lagrange point on the interface. As the discontinuous space $P^{k-1,dc}$ is defined in an element-wise manner, implementation is simplified. We can define one global pressure $p_h \in L_h$ and define fluid- and solid-pressure as restrictions:

$$p_{h,f} = p_h\Big|_{\mathcal{F}}, \quad p_{h,s} = p_h\Big|_{\mathcal{S}}.$$

For the definition of the test spaces, we need to pay special attention to the interface. While velocity and deformation are defined in a global way, only the test space $\phi \in \mathcal{V}$ for the momentum equation is defined on the complete domain Ω. The test functions for extension of the deformation $\psi_f \in \mathcal{W}_f$ as well as the test space for the deformation-velocity relation $\psi_s \in \mathcal{L}_s$ must be decoupled at the interface. Based on the second (just as example) choices of finite element spaces, we define

$$\begin{aligned}
V_h &:= \text{span}\{\phi_h \in C(\Omega)^d,\ \phi_h^{(i)} \text{ piece-wise quadratic},\ \phi_h = 0 \text{ on } \Gamma^D\},\\
W_h &:= \text{span}\{\phi_h \in C(\Omega)^d,\ \phi_h^{(i)} \text{ piece-wise quadratic } \phi_h = 0 \text{ on } \partial\Omega\},\\
L_{h,f} &:= \text{span}\{\xi_h \in L^2(\mathcal{F}),\ \xi_h^{(i)} \text{ piece-wise linear}\},\\
W_{f,h} &:= \text{span}\{\phi_h \in C(\mathcal{F})^d,\ \phi_h^{(i)} \text{ piece-wise quadratic } \phi_h = 0 \text{ on } \partial\mathcal{F}\}\\
L_{s,h} &:= \text{span}\{\phi_h \in C(\mathcal{S})^d,\ \phi_h^{(i)} \text{ piece-wise quadratic}\}.
\end{aligned} \tag{5.26}$$

With this construction of finite element spaces, we can define a well-posed discrete finite element approximation of the backward-Euler discretization for fluid-structure interactions in Arbitrary Lagrangian Eulerian coordinates:

Problem 5.12 (Finite Element Discretization of the fsi-System in ALE Formulation) *Let $A(\cdot,\cdot)$ be given by (5.10), $F(\cdot)$ by (5.11). The Jacobian $A(\mathbf{U})(\cdot,\cdot)$ is given by Theorem 5.2. Given the last discrete Newton approximation $\mathbf{U}_h^{(l-1)} \in X_h$, find*

$$\mathbf{W}_h^{(l)} := \{\mathbf{v}_h, \mathbf{u}_h, p_{f,h}\} \in X_h := V_h \times W_h \times L_{h,f},$$

such that

$$A'(\mathbf{U}_h^{(l-1)})(\mathbf{W}_h^{(l)}, \Phi_h) = F(\Phi_h) - A(\mathbf{U}_h^{(l-1)})(\Phi_h) \tag{5.27}$$

for all

$$\Phi_h := \{\phi_h, \psi_{h,f}, \psi_{h,s}, \xi_{h,f}\} \in Y_h := V_h \times W_{h,f} \times L_{h,s} \times L_{h,f}.$$

The Newton update problem in step (5.27) defines a linear system of equations. Chapter 7 will be devoted to the solution of this linear problem. First we note that for our choice of finite element spaces (5.26), the system of equations is quadratic, i.e., the number of unknowns equals the number of equations.

5.3.3 Stabilized Finite Elements for Fluid-structure Interactions

In Sect. 4.3.2, we have introduced concepts for stabilizing finite element pairs that do not satisfy the inf-sup condition. Here, we want to shortly apply this concept to the discretization of fluid-structure interactions. The basic idea was to either modify the test space by a Petrov-Galerkin approach, or to modify the variational formulation by adding stabilization terms $S_h(\cdot,\cdot)$. This latter approach is more general and also covers Petrov-Galerkin discretizations. We shortly discuss the very simple case of the non-conforming pressure stabilization used in Lemma 4.47. The linearized discrete variational formulation is enriched by a pressure stabilization term

$$A_h'(\mathbf{U}_h)(\mathbf{W}_h, \Phi_h) := A(\mathbf{U}_h)(\mathbf{W}_h, \Phi_h) + S_h(\mathbf{W}_h, \Phi_h).$$

For the proper definition of pressure stabilization in Arbitrary Lagrangian Eulerian formulation, we must transfer the standard method from Eulerian coordinates to the fixed reference system. Hence, let—just for the following discussion—$\hat{\mathcal{F}}$ be the reference fluid domain and $\mathcal{F}$ be the current Eulerian fluid-domain in the current time step. Then, the pressure stabilization term in Eulerian coordinates on $\mathcal{F}$ was defined as

$$S_h(\mathbf{U}_h, \Phi_h) := (\alpha_{\text{stab}} \nabla p_h, \nabla \xi_h)_{\mathcal{F}}, \tag{5.28}$$

with an element-wise defined stabilization parameter

$$\alpha_{\text{stab}}\Big|_K = \alpha_0 \left(\frac{\nu_f}{h_K^2} + \frac{\|\mathbf{v}\|_{L^\infty(K)}}{h_K} \right),$$

see Sect. 4.3.2. The mesh-size h_K would be the mesh-size of a Eulerian mesh. The first detail that has to be analyzed in the context of Arbitrary Lagrangian formulations is the concept of the mesh-size h_K. Usually, for shape-regular triangulations (see Definition 4.18), we can define the mesh-size of the triangulation $\hat{\Omega}_h$ of the reference domain $\hat{\mathcal{F}}$ as

$$\hat{h}_K := \operatorname{diam}(K). \tag{5.29}$$

Another suitable definition is to define the mesh-size as an integral value

$$\hat{h}'_K := \left(\int_K 1 \, \mathrm{d}x \right)^{\frac{1}{d}}. \tag{5.30}$$

On shape-regular triangulations, there exists a constant $c > 0$, such that

$$c^{-1} h'_K \leq h_K \leq c h'_K \quad \forall \hat{K} \in \hat{\Omega}_h, \quad (h \to 0). \tag{5.31}$$

In the following, we will use definition (5.30) by integration. Now, let $T : \hat{K} \to K$ be the ALE map and $K := T(\hat{K})$ be the Eulerian counterpart of $\hat{K} \in \hat{\Omega}_h$. It holds

$$h_K := \left(\int_K 1 \, \mathrm{d}x \right)^{\frac{1}{d}} = \left(\int_{\hat{K}} J \, \mathrm{d}\hat{x} \right)^{\frac{1}{d}},$$

and we can estimate

$$\min_{\hat{x} \in \hat{K}} |J(\hat{x})|^{\frac{1}{d}} \hat{h}_K \leq h_k \leq \max_{\hat{K}} |J(\hat{x})|^{\frac{1}{d}} \hat{h}_K. \tag{5.32}$$

Using this relation between Eulerian and reference mesh size, the stabilization term (5.28) can be transformed in ALE coordinates

$$S_h(\hat{\mathbf{U}}_h, \hat{\Phi}_h) = (\alpha_{\text{stab}} J \mathbf{F}^{-1} \mathbf{F}^{-T} \nabla p_h, \nabla \xi_h)_{\hat{\mathcal{F}}}.$$

with a stabilization parameter α_{stab} defined on $\hat{\mathcal{F}}$ as

$$\alpha_{\text{stab}} = \alpha_0 \left(\frac{\nu_f J^{\frac{2}{d}}}{\hat{h}_K^2} + \frac{\|\hat{\mathbf{v}}\|_{L^2(\hat{K})} J^{\frac{1}{d}}}{\hat{h}_K} \right)^{-1}.$$

If the deformation of the mesh is moderate, it holds $J \approx 1$ and $\mathbf{F} \approx I$. Then we can simply take the standard setting of the stabilization term (5.28) without any mapping.

This construction is also applicable for the stabilization by means of Local Projections as discussed in Lemma 4.49

$$S_{\text{lps}}(\hat{\mathbf{U}}_h, \hat{\Phi}_h) = \left(\alpha \mathbf{F}^{-1}\mathbf{F}^{-T}\nabla(p_h - \pi_h p_h), \nabla(\xi_h - \pi_h \xi_h)\right)_{\hat{\mathcal{F}}},$$

where $\pi_h : Q_h \to \tilde{Q}_h$ is the local coarse mesh projection operator. As in the Eulerian setting, the LPS method will give optimal order of convergence, if the spaces $\tilde{Q}_h$ and Q_h are well chosen, as weak consistency holds

$$p_h \in \tilde{Q}_h \quad \Rightarrow \quad S_{\text{lps}}(p_h, \xi_h) = 0 \quad \forall \xi_h \in Q_h.$$

In the case of residual based stabilization techniques like PSPG (or SUPG), the correct application to the Arbitrary Eulerian Lagrangian formulation is more difficult. The success of these techniques is based on a consistent formulation. If $\mathbf{U} \in \mathcal{X}$ is the solution, it should hold

$$S_{\text{PSPG}}(\mathbf{U}, \Phi_h) = 0 \quad \forall \Phi_h \in X_h.$$

This is realized by testing the complete momentum equation of the fluid system (compare the Jacobian in Theorem 5.2) with the modified test function

$$\tilde{\phi}_h := \phi_h + \alpha \nabla \xi_h.$$

Such a combination gives rise to complex coupled terms including the complete strong residual. For a discussion on a practical way of applying residual based stabilization techniques to fsi-problems in Arbitrary Lagrangian Eulerian coordinates, we refer to Wall [339].

Remark 5.13 (Stabilization for Large Deformations) As long as the deformation of the domain is small and motion of the domains is slow, we can apply all stabilization techniques without any modification and just omit the ALE mapping. This does not hold true, if the deformation is very large, i.e., if $J \ll 1$ or $J \gg 1$ or if $\mathbf{F}$ significantly differs from the identity I. As long as the ALE mapping is isotropic, we only need to adjust the mesh size by means of relation (5.32). If the mapping however inhibits very strong anisotropies, the concept of stabilization must be altered. In particular, it will be necessary to separate directions. On a Eulerian, Cartesian anisotropic mesh, the simple pressure stabilization term in the case of the linear Stokes equations must be constructed as:

$$S_{h,\text{aniso}}(\mathbf{U}_h, \Phi_h) = (\alpha_0 h_x^2 \partial_x p_h, \partial_x \xi_h)_{\mathcal{F}} + (\alpha_0 h_y^2 \partial_y p_h, \partial_y \xi_h)_{\mathcal{F}}.$$

For a detailed analysis of the Local Projection stabilization on anisotropic meshes, we refer to the Literature [58, 62, 277, 278] and in particular Molnar [247] in the case of fluid-structure interactions.

Besides stabilization of the pressure-velocity coupling, we need to take care of problems with dominant convection that require stabilization of transport oscillations. Here, we can follow the same procedure: starting with a stabilization technique in Eulerian coordinate, we map the resulting stabilization terms back to the reference framework. Again, all methods work very well without modifications, if small deformations are considered. Only the case of very large deformation with substantial anisotropies is still open. See [247, 339].

Apart from the natural convection, ALE formulations include the additional transport term

$$-\left(\rho_f J\mathbf{F}^{-1}\partial_t\mathbf{u}_f\cdot\nabla\mathbf{v},\phi\right)_{\mathcal{F}},$$

coming from the ALE time derivative. This term may call for stabilization, if the domain moves rapidly. Stabilization of this part can be handled like the natural convection by simply considering a combined effective transport velocity

$$\left(\rho_f J\mathbf{F}^{-1}\left(\mathbf{v}_f-\partial_t\mathbf{u}_f\right)\cdot\nabla\mathbf{v},\phi\right)_{\mathcal{F}},$$

5.3.4 Matrix Formulation of the Linear Systems

A finite element discretization of the linearized system to be solved in every step of the Newton iteration

$$\mathbf{W}_h\in X_h\quad A'(\mathbf{U}_h)(\mathbf{W}_h,\Phi_h)=F(\Phi_h)-A(\mathbf{U}_h)(\Phi_h)\quad\forall\Phi_h\in Y_h \tag{5.33}$$

gives rise to a large linear system of equations that can be compactly written in the form

$$\mathbf{A}_h\mathbf{x}_h=\mathbf{b}_h.$$

In this section, we will give details on the derivation and resulting structure of the system matrix. The exact form of the matrix will depend on the choice of finite element spaces. For the following discussion we make further assumptions on the finite element spaces:

- First, we assume that the triangulation is matching the domain-partitioning.
- We assume that both fluid and solid problem are given with Dirichlet conditions on the outer boundaries of the domain. In this case, it holds $\mathcal{V}=\mathcal{W}$ and it will also hold (in terms of (5.26)) that $V_h=W_h$.

- We consider inf-sup stable finite elements, such that no pressure-stabilization is required.
- We choose equal-order finite element spaces for velocity $\mathcal{V}$ and deformation $\mathcal{W}$, as well as for the test function of momentum equations $\mathcal{V}$, ALE extension $\mathcal{W}_f$ and deformation-velocity relation $\mathcal{L}_s$. All these discrete spaces are based on the same set of matrix-functions.

By these assumptions, let V_h be the space of continuous finite elements on the complete domain Ω_h of degree $r \geq 2$ with strong Dirichlet-values on the complete boundary $\partial\Omega_h$. The Lagrangian nodal basis is given by

$$V_h := \text{span}\{\phi_h^{(i)},\ i = 1, \ldots, N\}.$$

Discrete velocity update and deformation update are given by

$$\mathbf{z}_h(x) = \sum_{i=1}^{N} \mathbf{z}_i \phi_h^{(i)}(x), \quad \mathbf{w}_h(x) = \sum_{i=1}^{N} \mathbf{w}_i \phi_h^{(i)}(x).$$

We define the following subsets of indices that collect all basis functions with support in the fluid, in the solid and those that touch the interface

$$\begin{aligned} I_f &:= \{i \in \{1, \ldots, N\} \mid \text{supp}(\phi_h^{(i)}) \subset \mathcal{F}\}, \quad N_f := \#I_f, \\ I_s &:= \{i \in \{1, \ldots, N\} \mid \text{supp}(\phi_h^{(i)}) \subset \mathcal{S}\}, \quad N_s := \#I_s, \\ I_i &:= \{1, \ldots, N\} \setminus (I_f \cup I_s), \quad N_i := \#I_i. \end{aligned}$$

Then, the test space of the ALE-extension is given by

$$W_{h,f} := \text{span}\{\phi_h^{(i)},\ i \in I_f\},$$

and the test space of the deformation-velocity coupling by

$$W_{h,s} := \text{span}\{\phi_h^{(i)},\ i \in I_s \cup I_i\}.$$

Finally, the pressure-space $L_{h,f}$ is given by

$$L_{h,f} = \text{span}\{\xi_h^{(i)},\ i = 1, \ldots, N_p\}.$$

By $\xi_h^{(i)}$ a basis of either a lower-degree continuous space (e.g. $r-1$ on quadrilaterals), or some discontinuous space can be given. The pressure update is given by

$$q_{h,f}(x) = \sum_{i=1}^{N_p} \mathbf{q}_i \xi_h^{(i)}(x).$$

By insertion of these basis representations in (5.33), we derive the matrix formulation of the linear system. This matrix has a block-structure on multiple levels. First, parts of the equation act on the fluid-domain, parts on the solid-domain. Second, we get a natural block-structure due to the coupled equations: momentum equation of Navier-Stokes *(NS)*, divergence condition in the Navier-Stokes equations *(div)*, equation for the extension of the ALE map *(ALE)*, momentum equation of the elastic solid *(ES)* and finally, relation between deformation and velocity *(uv)*. Each of these equations appears in the Jacobian and may appear multiple times. The momentum part of the Navier-Stokes equations *(NS)* has directional derivatives with respect to the pressure, the velocity and the deformation. We will use this terminology to denote the sub-matrices and explain this procedure based on the Navier-Stokes momentum equations including the derivatives with respect to pressure and velocity:

$$
\begin{aligned}
[F_p^{NS}]_{ij} &= -\left(J\mathbf{F}^{-T}\xi_{h,f}^{(j)}, \phi_h^{(i)}\right)_{\mathcal{F}} \\
&\qquad \forall i \in I_f \cup I_i, \quad \forall j \in \{1, \ldots, N_p\} \\
[F_{\mathbf{v}}^{NS}]_{ij} &= \left(\rho_f J\left(k^{-1}\tilde{\phi}_{h,f}^{(j)} + \nabla\tilde{\phi}_{h,f}^{(j)}\mathbf{F}^{-1}\left(\mathbf{v} - \frac{\mathbf{u} - \mathbf{u}^{\text{old}}}{k}\right)\right), \phi_h^{(i)}\right)_{\mathcal{F}} \\
&\quad + \left(\rho_f J\nabla\mathbf{v}\mathbf{F}^{-1}\tilde{\phi}_{h,f}^{(j)}, \phi_h^{(i)}\right)_{\mathcal{F}} \\
&\quad + \left(J\frac{d\boldsymbol{\sigma}_f}{d\mathbf{v}}(\mathbf{W})\mathbf{F}^{-T}, \nabla\phi\right)_{\mathcal{F}} - \left(J\mathbf{F}^{-T}q_f, \nabla\phi\right)_{\mathcal{F}} \\
&\qquad \forall i \in I_f \cup I_i, \quad \forall j \in I_f \cup I_i
\end{aligned}
$$

All the remaining parts are obtained in a similar way. Altogether, we get the following matrices for fluid- and solid-problem:

$$
\mathbf{F} = \begin{pmatrix} 0 & F_{\mathbf{v}}^{div} & F_{\mathbf{u}}^{div} \\ F_p^{NS} & F_{\mathbf{v}}^{NS} & F_{\mathbf{u}}^{NS} \\ 0 & 0 & F_{\mathbf{u}}^{ALE} \end{pmatrix}, \quad \mathbf{S} = \begin{pmatrix} S_{\mathbf{v}}^{ES} & S_{\mathbf{u}}^{ES} \\ S_{\mathbf{v}}^{uv} & S_{\mathbf{u}}^{uv} \end{pmatrix}, \tag{5.34}
$$

with

$$
\mathbf{F} \in \mathbb{R}^{(N_p+2N_f+2N_i)\times(N_p+2N_f+2N_i)}, \quad \mathbf{S} \in \mathbb{R}^{(2N_s+2N_i)\times(2N_s+2N_i)}.
$$

To assemble the coupled system matrix on the complete domain Ω, we must construct the sum of both parts. First, we define subsets of the coefficient vectors

$$
\mathbf{z} = \{\mathbf{z}_f, \mathbf{z}_i, \mathbf{z}_s\}, \quad \mathbf{w} = \{\mathbf{w}_f, \mathbf{w}_i, \mathbf{w}_s\},
$$

where $\mathbf{z}_f$, $\mathbf{z}_i$ and $\mathbf{z}_s$ denote only indices in I_f, I_i and I_s, respectively. The same splitting is applied to $\mathbf{w}$ and also to the test functions ϕ_h and ψ_h. By this definition, we can give a more detailed version of the two sub-matrices that distinguishes between degrees freedom within the domain and those on the interface

$$\mathbf{F}_h = \begin{bmatrix} \xi_{h,f} \\ \phi_{h,f} \\ \psi_{h,f} \\ \phi_{h,i} \\ \psi_{h,i} \end{bmatrix} \begin{pmatrix} 0 & F_{\mathbf{v}}^{div} & F_{\mathbf{u}}^{div} & F_{\mathbf{v}}^{div} & F_{\mathbf{u}}^{div} \\ F_p^{NS} & F_{\mathbf{v}}^{NS} & F_{\mathbf{u}}^{NS} & F_{\mathbf{v}}^{NS} & F_{\mathbf{u}}^{NS} \\ 0 & 0 & F_{\mathbf{u}}^{ALE} & 0 & F_{\mathbf{u}}^{ALE} \\ F_p^{NS} & F_{\mathbf{v}}^{NS} & F_{\mathbf{u}}^{NS} & F_{\mathbf{v}}^{NS} & F_{\mathbf{u}}^{NS} \\ 0 & 0 & 0 & 0 & 0 \end{pmatrix}$$

$$\mathbf{S}_h = \begin{bmatrix} \phi_{h,i} \\ \psi_{h,i} \\ \phi_{h,s} \\ \psi_{h,s} \end{bmatrix} \begin{pmatrix} S_{\mathbf{v}}^{ES} & S_{\mathbf{u}}^{ES} & S_{\mathbf{v}}^{ES} & S_{\mathbf{u}}^{ES} \\ S_{\mathbf{v}}^{uv} & S_{\mathbf{u}}^{uv} & S_{\mathbf{v}}^{uv} & S_{\mathbf{u}}^{uv} \\ S_{\mathbf{v}}^{ES} & S_{\mathbf{u}}^{ES} & S_{\mathbf{v}}^{ES} & S_{\mathbf{u}}^{ES} \\ S_{\mathbf{v}}^{uv} & S_{\mathbf{u}}^{uv} & S_{\mathbf{v}}^{uv} & S_{\mathbf{u}}^{uv} \end{pmatrix}$$

We note that the off-diagonal blocks that indicate couplings between interface degrees of freedom with those inside the fluid-domain are mainly zero, as only very few basis functions $\phi_{h,i}$ and $\phi_{h,f}$ have an overlapping support. The saddle-point structure of the Navier-Stokes equations is directly visible. Finally, we note that the test space for the ALE extension $W_{h,f}$ does not include test functions that live on the interface. This is the correct choice, as the ALE map is defined as an extension of the solid's deformation by using Dirichlet values. Nevertheless, this last row is included in $\mathbf{F}_h$ to yield a quadratic matrix.

Given this detailed description of the sub-matrices, we can formulation the coupled linear system of equations by the sum of the two sub-systems:

$$\mathbf{A} = \begin{pmatrix} F_p^{div} & F_{\mathbf{v}}^{div} & F_{\mathbf{u}}^{div} & F_p^{div} & F_{\mathbf{v}}^{div} & F_{\mathbf{u}}^{div} & 0 & 0 \\ F_p^{NS} & F_{\mathbf{v}}^{NS} & F_{\mathbf{u}}^{NS} & F_p^{NS} & F_{\mathbf{v}}^{NS} & F_{\mathbf{u}}^{NS} & 0 & 0 \\ 0 & 0 & F_{\mathbf{u}}^{ALE} & 0 & 0 & F_{\mathbf{u}}^{ALE} & 0 & 0 \\ F_p^{div} & F_{\mathbf{v}}^{div} & F_{\mathbf{u}}^{div} & F_p^{div} & F_{\mathbf{v}}^{div} & F_{\mathbf{u}}^{div} & 0 & 0 \\ F_p^{NS} & F_{\mathbf{v}}^{NS} & F_{\mathbf{u}}^{NS} & F_p^{NS} & F_{\mathbf{v}}^{NS} + S_{\mathbf{v}}^{ES} & F_{\mathbf{u}}^{NS} + S_{\mathbf{u}}^{ES} & S_{\mathbf{v}}^{ES} & S_{\mathbf{u}}^{ES} \\ 0 & 0 & 0 & 0 & S_{\mathbf{v}}^{uv} & S_{\mathbf{u}}^{uv} & S_{\mathbf{v}}^{uv} & S_{\mathbf{u}}^{uv} \\ 0 & 0 & 0 & 0 & S_{\mathbf{v}}^{ES} & S_{\mathbf{u}}^{ES} & S_{\mathbf{v}}^{ES} & S_{\mathbf{u}}^{ES} \\ 0 & 0 & 0 & 0 & S_{\mathbf{v}}^{uv} & S_{\mathbf{u}}^{uv} & S_{\mathbf{v}}^{uv} & S_{\mathbf{u}}^{uv} \end{pmatrix} \tag{5.35}$$

Again, we note that all the shaded matrix entries are very sparse. In every step of the Newton method we have to find the coefficient vector

$$\mathbf{x} = \left(\mathbf{q},\, \mathbf{z}_f,\, \mathbf{w}_f,\, \mathbf{z}_i,\, \mathbf{w}_i,\, \mathbf{z}_s,\, \mathbf{w}_s\right)^T \in \mathbb{R}^{N_p+2N_f+2N_i+2N_s},$$

subject to the linear system of equations

$$\mathbf{A}_h \mathbf{x} = \mathbf{b},$$

where $\mathbf{b}$ is the discrete right hand side, coming from the discretization of

$$G(\Phi) := F(\Phi) - A(\mathbf{U})(\Phi).$$

The system matrix $\mathbf{A}_h$ lacks all desirable properties like symmetry, positivity or diagonal dominance. Solution of these linear systems is a very difficult task. Application of direct solvers is problematic due to the immense dimension of the linear system. Furthermore, we will see in Chap. 7, that the condition number of the coupled matrix can be so bad that even modern direct solvers can fail.

5.3.5 Construction of the ALE Map

In this section, we demonstrate different ways of extending the solid deformation $\mathbf{u}_{h,s}$ from the interface to the fluid domain $\mathbf{u}_{h,f}$. Such an extension is the typical way for defining the ALE mapping by means of

$$T_{h,f}(x,t) := x + \mathbf{u}_{h,f}(x,t).$$

Here, we aim at a quantitative comparison of different mesh motion models. In Sect. 3.5.1, we have already discussed qualitative regularity restrictions that arise from different mesh motion models. Further computational overviews are given in the literature [342, 357].

We will analyze a simple numerical test case that gives rise to large rotations of an unsupported solid in a fluid domain. This rotation causes very large deformation of the fluid domain an poses severe challenges to the construction of the ALE map. We show the configuration of the geometry in Fig. 5.13a. We briefly detail the configuration. The initial domain partitioning is given as

$$\Omega = (-1,1)^2,\ \hat{\mathcal{S}} = \left(-\frac{1}{2},\frac{1}{2}\right) \times \left(-\frac{1}{8},\frac{1}{8}\right),\ \hat{\mathcal{F}} = \Omega \setminus \overline{\hat{\mathcal{S}}}.$$

The boundary $\Gamma = \partial\Omega$ consists of two inflow parts of width 0.5, Γ_1^{in} in the upper left corner and Γ_2^{in} in the lower right one. Here we prescribe a Dirichlet condition for the velocity

$$\mathbf{v}_i^{\text{in}}(x,y,t) = 4\alpha(t)(x - x_i^0)(x - x_i^1)\mathbf{n}_i \text{ on } \Gamma_i^{\text{in}},$$

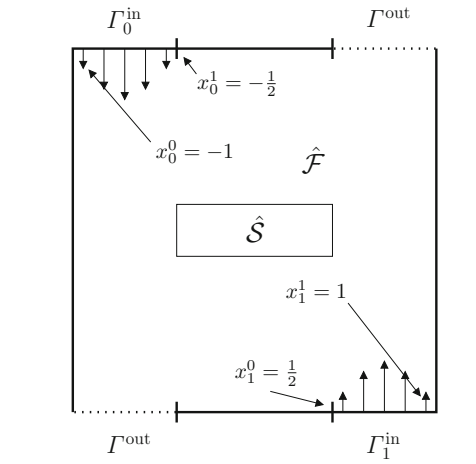

(a)

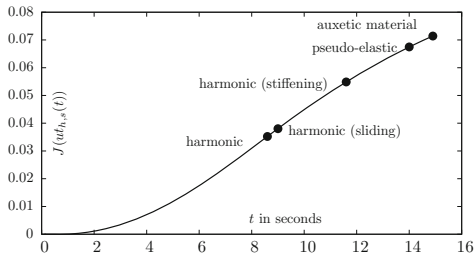

(b)

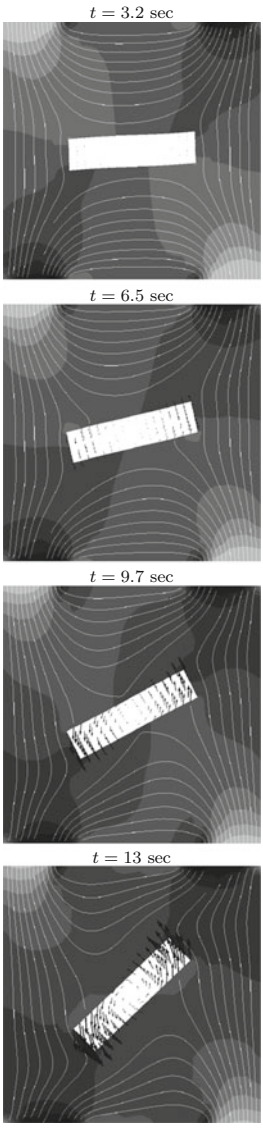

(c)

Fig. 5.13 Description of the benchmark problem for testing the influence of the ALE map definition. (**a**) Geometric configuration of the test case. The boundary consists of two inflow, two outflow parts and a rigid wall. The solid $\hat{\mathcal{S}}$ is not supported. The domain Ω is split into fluid $\hat{\mathcal{F}}$ and solid $\hat{\mathcal{S}}$ $\Omega = (-1, 1)^2$, $\hat{\mathcal{S}} = \left(-\frac{1}{2}, \frac{1}{2}\right) \times \left(-\frac{1}{8}, \frac{1}{8}\right)$, $\hat{\mathcal{F}} = \Omega \setminus \overline{\hat{\mathcal{S}}}$. On the two inflow boundary parts Γ_i^{in} $(i = 1, 2)$ we prescribe parabolic Dirichlet conditions for the velocity $\mathbf{v}_f$. (**b**) Rotation $J(\mathbf{u}_{h,s}(t))$ as function over time indicating the rigid body rotation of the solid. The *points* indicate the final time, where mesh elements start to deteriorate. (**c**) *Right*: Solution at different times with streamlines and deformation vector field. *Bright colors* indicate large pressure, *dark colors* indicate small pressures

where the x_i^j are indicated in the sketch of the configuration and where $\mathbf{n}_i$ is the outward facing normal vector at Γ_i^{in}. The function $\alpha(t)$ is added for a smooth initial transition

$$\alpha(t) = \begin{cases} \frac{1}{2}\left(1 - \cos(\pi t/2)\right) & t \leq 2\,\text{s}, \\ 1 & t \geq 2\,\text{s} \end{cases}.$$

The solid is modeled as St. Venant-Kirchhof material. All parameters are given as

$$\rho_f = 1\,\text{kg}\cdot\text{m}^{-3}, \quad \rho_s = 1000\,\text{kg}\cdot\text{m}^{-3},$$
$$\mu_s = 20\,\text{kg}\cdot\text{m}^{-1}\text{s}^{-2}, \quad \lambda_s = 80\,\text{kg}\cdot\text{m}^{-1}\text{s}^{-2}, \quad \nu_f = 1\,\text{m}^2\cdot\text{s}^{-1}.$$

In the right plot of Fig. 5.13c, we show the solution at different points in time. Bright values denote large pressures, dark colors small ones. Further, we plot streamlines of the velocity field and the vector field of the solid deformation. The symmetric flow causes a rotational movement of the solid. As quantity of interest, we measure the average rotation

$$J(\mathbf{u}_h(t)) = \frac{1}{|\hat{\mathcal{S}}|}\int_{\hat{\mathcal{S}}} \hat{x} \times \mathbf{u}_{h,s}\,\mathrm{d}\hat{x}. \tag{5.36}$$

The value of $J(\mathbf{u}_h(t))$ is shown in Fig. 5.13b. Due to very large deformation of the fluid domain and a deterioration of the ALE map, all computations will break down at some final time $t' > 0$. These points in time are indicated in Fig. 5.13b. We will see that depending on the type of extension operator, we achieve a substantial difference in the final time.

5.3.5.1 Harmonic Extension

We start by defining the extension of the solid deformation $\mathbf{u}_{h,s}$ from the interface $\hat{\mathcal{I}}$ to the fluid-domain $\mathbf{u}_{h,f} \in V_{h,f}^{\Gamma}$, by means of an harmonic extension, given as

$$(\nabla \mathbf{u}_{h,f}, \nabla \psi_{h,f})_{\mathcal{F}} = 0 \quad \forall \psi_{h,f} \in W_{h,f}^{\Gamma}, \tag{5.37}$$

where $\psi_{h,f}$ has trace zero on the complete boundary of $\mathcal{F}$, that includes the interface. Solution $\mathbf{u}_{h,f}$ and test function $\psi_{h,f}$ come from standard finite element space with the boundary constraints

$$\begin{aligned} \mathbf{u}_{h,f} \in V_{h,f}^{\Gamma} &:= \{\phi_h \in V_h(\mathcal{F}),\ \phi_h = \mathbf{u}_{h,s} \text{ on } \mathcal{I},\ \phi_h = 0 \text{ on } \partial\mathcal{F} \setminus \mathcal{I}\} \\ \psi_{h,f} \in W_{h,f}^{\Gamma} &:= \{\phi_h \in V_h(\mathcal{F}),\ \phi_h = 0 \text{ on } \mathcal{I},\ \phi_h = 0 \text{ on } \partial\mathcal{F} \setminus \mathcal{I}\}. \end{aligned} \tag{5.38}$$

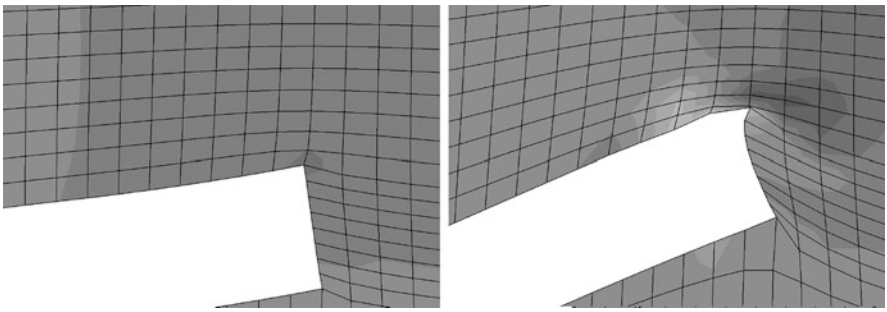

Fig. 5.14 Extension with the harmonic operator. *Left*: $t = 5$ s. *Right*: $t = 8.6$ s close to breakdown due to degeneration of map elements

We show results in Fig. 5.14 for two different points in time. While the ALE mapping yields a nicely transformed mesh at time $t = 5$ s, some elements are close to deterioration at time $t = 8.6$ s. This in particular happens at the edge of the solid. Here, we also see a very strong (and non-physical) feedback from the deformation to the elasticity problems. Bad approximation on strongly deformed meshes gives rise to artificial forces bending the solid.

This extension operator can be relaxed by varying the boundary conditions on the outer boundary

$$\Gamma_f := \partial\mathcal{F} \setminus \mathcal{I}.$$

Here, it is not strictly necessary for $\mathbf{u}_{h,f}$ to guarantee a full homogenous Dirichlet condition. If the deformation $\mathbf{u}_{h,f}$ is allowed to move freely in tangential direction, the resulting map $T_{h,f}$ will still map the reference domain to the fluid-domain. Hence, we can alter the test space $W_{h,f}$ in such a way that Dirichlet-conditions are only imposed in normal direction, similar to the free-slip condition that is known from fluid-dynamics

$$W_{h,f}^{\Gamma} := \{\phi \in C(\mathcal{F})^d, \phi_h\Big|_K \in P^r(K),\ \mathbf{n} \cdot \phi_h = 0 \text{ on } \Gamma_f,\ \phi_0 = 0 \text{ on } \mathcal{I}\},$$

where $P^r(K)$ is the local finite element space. In Fig. 5.15 we show both different choices of boundary values. Although we choose different boundary values only on the outer boundary of the domain, we see a substantial improvement of mesh quality at the interface. In particular, the solid's shape is not deteriorated at the edges. However, some mesh elements already start to lose regularity.

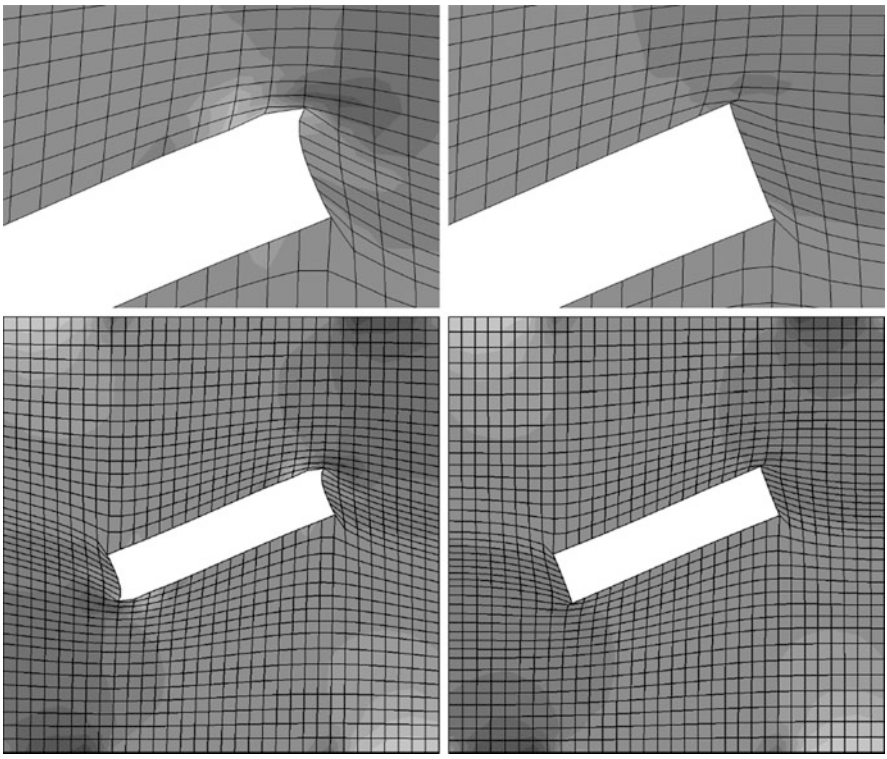

Fig. 5.15 Extension with the harmonic operator. Comparison of different boundary values at the outer boundary $\partial\mathcal{F} \setminus \mathcal{I}$. *Left*: homogenous Dirichlet $\mathbf{u}_{h,f} = 0$. *Right*: $\mathbf{n} \cdot \mathbf{u}_{h,f} = 0$. Both at times $t = 8.6\,\mathrm{s}$. In the *bottom line* we show the complete computational domain. Here, the effect of sliding boundary conditions gets obvious

5.3.5.2 Harmonic Extension with Stiffening

The examples show that we have to expect difficulties close to the solid domain, in particular close to edges. Here, stiffening of the extension can help to assure better quality of the deformed meshes. We change the extension operator by introducing a local parameter function $\alpha : \mathcal{F} \to \mathbb{R}_+$:

$$(\alpha \nabla \mathbf{u}_{h,f}, \nabla \phi_{h,f})_{\mathcal{F}} = 0 \quad \forall \psi_{h,f} \in W^{\Gamma}_{h,f}.$$

Given differentiability of $\alpha(x)$, this weak formulation belongs to a transport-diffusion problem

$$-\Delta \mathbf{u}_{h,f} - \alpha^{-1} \nabla \alpha \cdot \nabla \mathbf{u}_{h,f} = 0.$$

If we can choose $\alpha : \mathcal{F} \to \mathbb{R}_+$ in such a way that the ratio

$$\frac{|\nabla \alpha|}{|\alpha|} \gg 0 \text{ at } \mathcal{I},$$

is large close to the interface, and if the transport direction points away from the interface

$$-\nabla \alpha \sim \mathbf{n}_s \text{ at } \mathcal{I},$$

where $\mathbf{n}_s$ is the outward facing normal vector of $\mathcal{S}$, the extension mainly behaves like a simple transport-problem and the deformation $\mathbf{u}_{h,s}$ on $\mathcal{I}$ is carried into the fluid-domain with as little changes as possible. Further away from the interface, the extension should take the role of a harmonic extension. The choice of $\alpha(x)$ can be based on the distance of x to the nearest interface point

$$d_{\mathcal{I}}(x) := \min_{y \in \mathcal{I}} \|x - y\|_2.$$

A good choice of α is

$$\alpha(x) = 2.0 - \operatorname{erf}\left(5 d_{\mathcal{I}}(x)\right),$$

where erf is the Gauss error function. For this choice of α it holds

$$\frac{|\nabla \alpha(x)|}{|\alpha(x)|} > 1 \text{ if } d_{\mathcal{I}}(x) < \frac{1}{4} \text{ and } \frac{|\nabla \alpha(x)|}{|\alpha(x)|} \ll \frac{1}{100} \text{ if } d_{\mathcal{I}}(x) > \frac{1}{2}.$$

By a proper scaling of this function, the area of dominant transport can be adjusted to the specific geometry. Figure 5.16 shows the results. First, we see a significant improvement in mesh-quality. If we go on in time and rotation, we again see deterioration of mesh elements and also a non-physical deformation of the solid. We could already increase the final time, where the ALE formulation will loose its regularity by about 20%.

5.3.5.3 Extension by Pseudo-Elasticity

Another possibility for defining the extension operator is by means of the Navier-Lamé equation, see also [296]

$$\left(\mu_e(\nabla \mathbf{u}_{h,f} + \nabla \mathbf{u}_{h,f}^T) + \lambda_e \operatorname{div} \mathbf{u}_{h,f} I, \nabla \psi_{h,f}\right)_{\mathcal{F}} = 0 \quad \forall \psi_{h,f} \in W_{h,f}^{\Gamma}.$$

The parameters μ_e and λ_e can again be chosen in such a way that the material stiffens closer to the solid. Let $E_e(x)$ be the Young modulus, depending on the

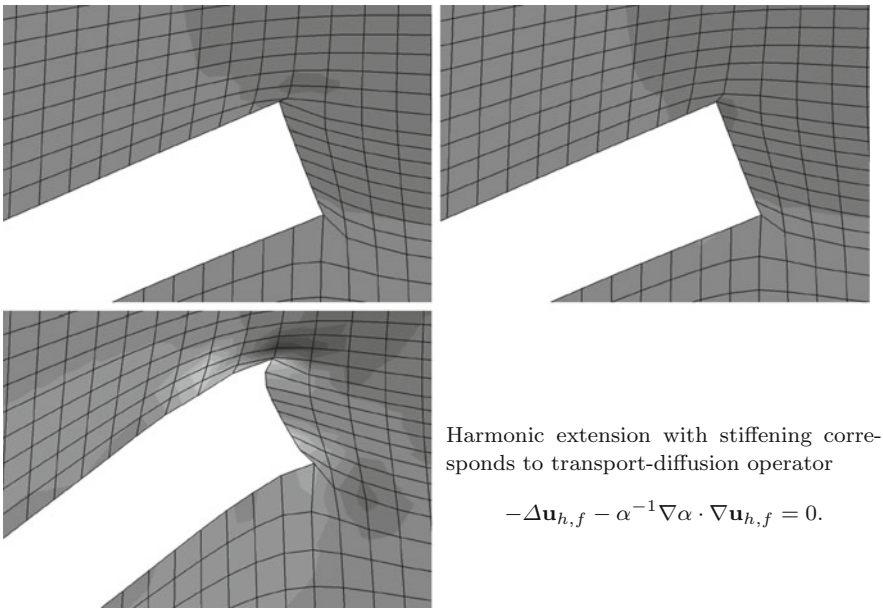

Fig. 5.16 *Upper row*: extension with the harmonic operator using sliding boundary conditions (*left*) and the harmonic operator with stiffening at the solid (*right*), both at time $t = 8.6$ s. *Lower row*: harmonic extension with stiffening at time $t = 11.6$ s

distance, and ν_e a chosen Poisson ratio. We pick the two parameters as

$$\mu_e(x) = \frac{E_e(x)}{2(1+\nu_e)}, \quad \lambda_e(x) = \frac{\nu_e E_e(x)}{(1+\nu_e)(1-2\nu_e)}.$$

The results at times $t = 11.6$ s and $t = 14$ s are shown in Fig. 5.17. At time 11.6 s we get a very good mesh quality (compared to the harmonic operator with stiffening). No artificial feedback to the solid problem is observed. The computations break down around $t = 14$ s.

Using the pseudo-elasticity model, one can improve the results by using material parameters in the *auxetic* range

$$-1 < \nu_e < 0.$$

Here, we pick $\nu_e = -0.2$. The results are shown in the lower right plot of Fig. 5.17. A significant improvement in mesh quality is not visible, but using material parameters in the auxetic range allows to reach a final time of $t = 14.9$ s.

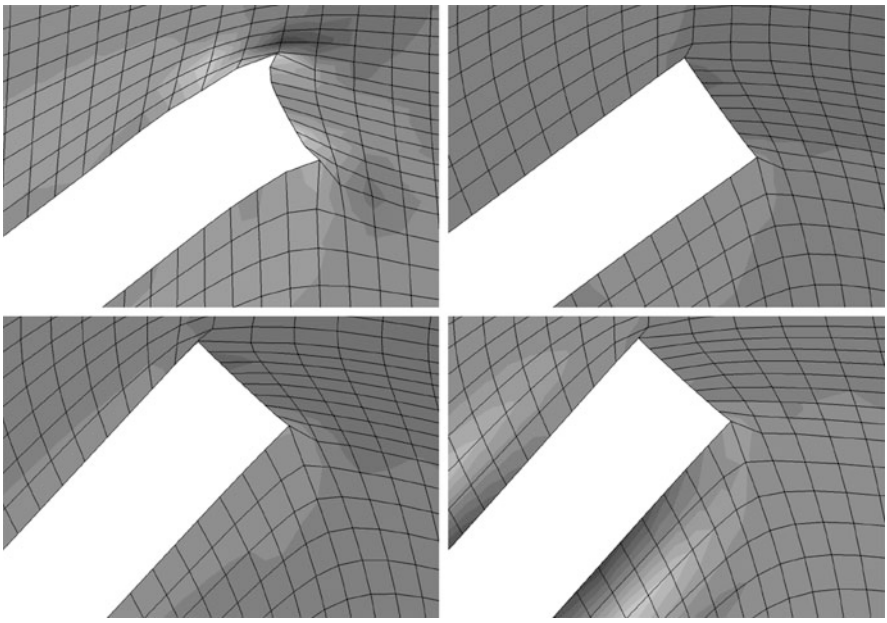

Fig. 5.17 *Upper row*: extension with the harmonic operator using stiffening (*left*) and using a pseudo-elasticity model (*right*), both at time $t = 11.6$ s. *Lower row*: pseudo-elastic extension at time $t = 14$ s (*left*) and pseudo-elasticity with an auxetic material behavior (*right*)

For a pseudo-elastic extension, it is possible to apply stiffening in a semi-automatic way, by coupling the Young modulus to the deformation gradient's determinant

$$J_e := \det(I + \nabla \mathbf{u}_h).$$

E_e is increased, if J_e gets large or close to zero:

$$E_e := E_e \left(J_e + \frac{1}{J_e} \right).$$

This technique is referred to as Jacobian-based stiffening, see [318].

5.3.5.4 Biharmonic Extension

Finally, we consider the biharmonic operator Δ^2 for defining the extension of the deformation, see also [182]. For realization, we choose a mixed formulation by

introducing a secondary variable $\mathbf{w}_f = -\Delta \mathbf{u}_f$:

$$(\nabla \mathbf{w}_{h,f}, \nabla \psi^1_{h,f})_{\mathcal{F}} + (\nabla \mathbf{u}_{h,f}, \nabla \psi^2_{h,f})_{\mathcal{F}} - (\mathbf{w}_{h,f}, \psi^2_{h,f})_{\mathcal{F}} = \langle \mathbf{n} \cdot \nabla \mathbf{u}_{h,s}, \psi^2_{h,f} \rangle_{\mathcal{I}},$$

where solution and test function come from the spaces

The biharmonic extension has the benefit that no configuration dependent parameter-tuning is necessary. Due to the fourth order character, special care has to be taken for discretization. Either, C^1-conforming finite elements, or a mixed formulation is required. For numerical benchmark problems, a very high computational effort is reported [342], with computing times up to ten times higher than for the simple harmonic extension. Hence, it is usually more advisable to spend some effort on parameter tuning and a good parameter choice for one of the previously discussed options.

5.3.5.5 Summary and Conclusion

In Table 5.2 we summarize the results from the previous section. The effect of the different methods for extending the deformation to the fluid domain and for generation of the ALE map are striking. Compared to the most simple harmonic extension, advanced techniques that are based on pseudo-elasticity can give good results for nearly twice as large deformations. Apart from the biharmonic operator all of these techniques have a comparable computational effort. Even if nonlinear models are used for stiffening, the effort for the solution of the extension problem is still negligible compared to the fluid and the solid problem.

Remark 5.14 (Alternative Approaches for Defining the ALE Map) All methods presented in this section have a similar type and based on the implicit inversion of a differential operator. This approach is natural for monolithic models, where fluid problem solid problem and mesh problem are formulated as one coupled system. Using partitioned algorithms it is easier to utilize different processed for designing the ALE map. Basting and co-workers [30] introduced the *extended ALE method* that is based on a variational mesh optimization scheme [294] that generates

Table 5.2 Final time for the breakdown of the ALE scheme for different types of ALE extension

Mesh motion model	Maximum time	Maximum rotation J
Harmonic	8.6 s	0.035
Harmonic (sliding)	9.0 s	0.038
Harmonic (stiffening)	11.6 s	0.055
Pseudo-elastic	14.0 s	0.067
Auxetic material	14.9 s	0.071

We also indicate the maximum value that has been reached for the rotation functional 5.36

distribution of the mesh nodes whenever the ALE map deteriorates. As an important feature to allow for efficient simulations the mesh connectivity is always preserved.

Schäfer et al. [300] block structure the computational mesh to allow for different mesh motion techniques in different parts depending on the distance to the elastic obstacle and the expected deformation. Among the applied techniques they also use linear interpolations to construct mesh distortions. In a monolithic setting this approach would cause global couplings in the matrix. As part of partitioned approaches this technique is very efficient.